

---

# Latent Style-based Quantum Wasserstein GAN for Drug Design

Julien Baglio<sup>1,2,\*</sup>, Yacine Haddad<sup>3,4,\*</sup> and Richard Polifka<sup>2</sup>

<sup>1</sup>Center for Quantum Computing and Quantum Coherence (QC2), Department of Physics, University of Basel, Klingelbergstrasse 82, CH-4056 Basel, Switzerland

<sup>2</sup>QuantumBasel, Schorenweg 44b, CH-4144 Arlesheim, Switzerland

<sup>3</sup>Laboratory for High Energy Physics (LHEP), Physics Institute, Faculty of Sciences, University of Bern, Sidlerstrasse 5, CH-3012 Bern, Switzerland

<sup>4</sup>Open Quantum Institute and Quantum Technology Initiative, CERN, Esplanade des Particules 1, CH-1211 Geneva 23, Switzerland

Correspondence\*:

julien.baglio@unibas.ch

yacine.haddad@unibe.ch

## ABSTRACT

The development of new drugs is a tedious, time-consuming, and expensive process, for which the average costs are estimated to be up to around \$2.5 billion. The first step in this long process is the design of the new drug, for which de novo drug design, assisted by artificial intelligence, has blossomed in recent years and revolutionized the field. In particular, generative artificial intelligence has delivered promising results in drug discovery and development, reducing costs and the time to solution. However, classical generative models, such as generative adversarial networks (GANs), are difficult to train due to barren plateaus and prone to mode collapse. Quantum computing may be an avenue to overcome these issues and provide models with fewer parameters, thereby enhancing the generalizability of GANs. We propose a new style-based quantum GAN (QGAN) architecture for drug design that implements noise encoding at every rotational gate of the circuit and a gradient penalty in the loss function to mitigate mode collapse. Our pipeline employs a variational autoencoder to represent the molecular structure in a latent space, which is then used as input to our QGAN. Our baseline model runs on up to 15 qubits to validate our architecture on quantum simulators, and a 156-qubit IBM Heron quantum computer in the five-qubit setup is used for inference to investigate the effects of using real quantum hardware on the analysis. We benchmark our results against classical models as provided by the MOSES benchmark suite.

**Keywords:** drug design, smiles, artificial intelligence, latent space, variational auto-encoder, quantum machine learning, quantum generative adversarial networks, superconducting-qubit quantum computer

## 1 INTRODUCTION

The development of new pharmaceutical drugs is a lengthy, tedious, and expansive process. It takes usually 15 years, and the lower estimate of mean expense is around \$1.3 billion<sup>1-4</sup>, and can rise up to around \$2.5 billion<sup>5,6</sup>. The development cycle consists of the following main stages: target discovery, molecular design, preclinical studies, clinical trials, and finally the regulatory approval to enter the market. In the first two stages, there exist two key strategies for identifying viable drug candidates: either by modifying already existing commercial drugs, for example by performing a virtual screening, or by identifying new relationships between already known molecular structures and the desired activity; or by generating entirely new molecules, also called de-novo drug design. In both methods there are multiple challenges, such as the safety of the candidate molecule, the efficiency, and eventually the ability to manufacture the drug candidate.

In this context, the emergence of artificial intelligence (AI) has revolutionized the drug design approach, in particular the advances of generative AI which has been used for computer-assisted drug design in the past decade<sup>7-9</sup>. Generative Adversarial Networks (GAN)<sup>10</sup> are prominent AI models applied for drug design<sup>11,12</sup>. A GAN is composed of two neural networks: 1) a generator, which is trained to create new molecular structures from random noise input distribution; 2) a discriminator, which is trained to classify between the generator (fake) output, and the (real) molecular structures contained in the train input dataset.

The training scheme is an adversarial game, where the generator aims to fool the discriminator as much as possible while the discriminator aims to distinguish between real data and newly generated fake data, which in turn will help the generator to perform better. While GANs (and more generally AI models for drug design) have blossomed in the past decade, their training can be computationally expensive when their scale is very large, and the associated massive parameter space requires careful optimization<sup>11</sup>. GANs can suffer from a non convergence of the adversarial training procedure, mode collapse when the generator only generates a sub-sample of the entire diversity of the molecules present in the training set, or falling into a non-robust training pattern with a great sensitivity to the hyperparameters of the models and to the initialization of the model weights.

Quantum machine learning aims to provide new avenues to overcome some of these challenges. Quantum generative models<sup>13–17</sup> are generative models relying on the rules of quantum mechanics: Starting from quantum states encoding the problem, subject to the rules of superposition and entanglement, they build up the final probabilistic output distribution using quantum measurements. Using spectral analysis, it has been shown that quantum neural networks probe different frequency modes compared to their classical counterparts, a feature which seems to be linked to higher expressivity of quantum machine learning<sup>18–21</sup>. Quantum GANs (QGANs)<sup>22–27</sup> thus offer new avenues for powerful generative neural networks and have been applied to drug design<sup>28–31</sup>. In<sup>30,31</sup> the authors have adopted the Wasserstein distance as the backbone of the loss function (WGAN)<sup>32</sup>, leading to an improvement over the early QGAN investigations for drug discovery<sup>28,29</sup>. In<sup>31</sup> this was also supplemented by gradient penalty (WGAN-GP)<sup>33</sup> to improve trainability. In<sup>30,31</sup> the quantum architecture was a modification of the MolGAN architecture<sup>34</sup>, the standard in computer-assisted drug design, and the two studies applied their quantum models on dataset of small molecules, QM9 dataset<sup>35</sup> and PC9 dataset<sup>36</sup>.

In this work we propose two improvements: 1) going beyond small-molecule generation and 2) investigating several modifications over the previous QGAN studies which enable a new state of the art for QGAN in computer-assisted drug design. First, we use the MOSES dataset and benchmark suite<sup>37</sup>, which is an industry-relevant dataset of SMILES molecules<sup>38</sup> not restricted to small molecules. In addition, aiming to exploit potential quantum advantages for sampling efficiency and model expressiveness and to address the challenge of mode collapse, we introduce a latent space approach in the quantum computing pipeline, following classical GAN studies for drug design<sup>39</sup>. The input SMILES molecules of the training dataset are projected into an abstract vector space on which the training is done, before decoding the output back to the practical, physical space. Our last improvement over previous quantum studies is the combination of this latent-space approach with a hybrid style-based quantum GAN<sup>40,41</sup> which uses data re-uploading, where the input noise distribution for the generator is inserted in all layers and not only in the first initial layer of the neural network. The style architecture was introduced for classical GAN in the context of image generation<sup>42</sup> and the latent style-based QGAN using WGAN-GP has been successfully tested for image generation<sup>43</sup> but never investigated for drug design. It should also be noted that the barren plateaus, where vanishing gradients render the training exponentially harder in the exploration of the loss function landscape, are less problematic when using the latent style-based approach for QGAN<sup>43</sup>. In addition, a recent study hinted towards a potential quantum exponential advantage with style-based QGAN in the number of trainable parameters<sup>44</sup>: an exponentially smaller number of trainable parameters for QGANs compared to their classical counterpart, a feature which is of high interest for a complex computer-assisted drug design pipeline.

The molecular structure is encoded following the SMILES approach. The SMILES strings are embedded into vectors of real numbers which are fed into the autoencoder projecting these vectors into an abstract latent vector space. The discriminator remains classical and we only use a parametrized quantum circuit for the generator. We benchmark our new quantum drug design architecture against classical latent GAN approach based on the widely used MOSES benchmark suite and show that our proposed latent style-based QGAN can be very efficient for drug design with far fewer trainable parameters than their classical counterparts. Our pipeline uses RDKit<sup>45</sup> to check that the new generated molecular structures from our pipeline do correspond to valid (bio)chemical compounds and to calculate relevant metrics. The training of our quantum computing pipeline is performed on noiseless quantum simulator, including the sampling of 30,000 new molecules to validate the pipeline. We also perform the sampling of 2,500

new, viable molecular structures on `ibm_kingston`, a 156-qubit IBM Heron quantum computer, using the model trained on quantum simulator. Using MOSES benchmark suite, we also quantify the quality of our output with metrics such as internal diversity, molecular weight, LogP, or quantitative estimation of drug-likeness. Our proposed quantum pipeline, tested on a real-world dataset not restricted to small molecules, greatly enhances the explainability of computer-assisted drug design by using far less trainable parameters than conventional classical AI pipeline for drug discovery. The statistical overall score of our pipeline demonstrates that it is competitive with classical AI pipeline, with even statistically significant improvements over classical GANs for some of the individual metrics we have investigated.

## 2 MATERIALS AND METHODS

### 2.1 Dataset construction

We use the MOSES dataset<sup>37</sup> as our main analysis dataset. This dataset is built out of the ZINC Clean Leads collection<sup>46</sup> and contains over 1.9M molecules of interest for biochemistry applications. We have further applied a random sampling of the dataset to obtain 12,000 molecules for training and 4,087 molecules for validation.

The reason for this downsize of the original MOSES dataset is two-fold: 1) we can test the small-dataset regime and show the capabilities of quantum-computing-assisted pipeline to perform well on small datasets; 2) in the proof-of-concept phase of our new quantum architecture, it helps to validate the concept within a short runtime. The MOSES dataset is a high-dimensional dataset which is currently not practical to be used directly on a quantum computer, due to limited availability of resources of current quantum hardware. We thus pre-process the data by transforming the SMILES strings into high-dimensional molecular descriptors using RDKit features<sup>45</sup>, which will be used for calculating the various metrics. The SMILES strings are then fed to an auto-encoder, see below, to compress the (high-dimensional) molecular alphabet into a latent representation (low-dimensional features), which is in turn compact enough to be used for the quantum part of our pipeline. The decoder part of the auto-encoder allows to map the generated latent features back into valid SMILES molecules. In order to check the chemical properties of the both the randomly selected samples for our final training and testing dataset as well as the generated samples, we have used RDKit filters<sup>45</sup>. Our procedure balances chemical validity, through the auto-encoder and the RDKit validation, with quantum feasibility allowed by the low-dimensional latent-feature encoding.

When generating new molecules, we have sampled 30,000 molecules unless stated otherwise, following the default value used in the MOSES benchmark suite.

### 2.2 Description of the pipeline

The structure of the molecules contained in our dataset is encoded using SMILES strings<sup>38</sup>. A standard method in classical generative approach for drug design uses a pre-trained auto-encoder to project the SMILES strings into a compact latent space, which is much more tractable than the original strings for the generative models. Note that the very first step before the auto-encoder is the extraction of chemical features from the SMILES strings using RDKit<sup>45</sup> in order to get the relevant metrics. The auto-encoder captures salient chemical features while reducing dimensionality, allowing to operate in a manageable latent representation. Following this approach also used in the MOSES benchmark suite, our pipeline starts with a pre-trained Variational Auto-Encoder (VAE) to encode the drug-like SMILES molecules into the latent space.

To perform the generation of new molecules we use a Generative Adversarial Network (GAN)<sup>10</sup>. A GAN is composed of two networks competing against each other: a generator, sampling new candidates from a random number input distribution; and a discriminator, acting as a binary classifier trained to distinguish between real input data and generated samples from the generator. The training is an adversarial procedure, a two-player minmax game between the two networks, until ideally a Nash equilibrium is reached, when the generator has become so good that the discriminator cannot distinguish anymore between real input data and generated samples. We will compare the classical GAN implementation as provided in the MOSES benchmark suite against our proposed quantum GAN architecture.

Quantum computing is a different paradigm to perform computations. Instead of the classical bits which have binary outcomes (0 or 1), quantum computers use qubits (quantum bits) which are quantum states of a controlled two-level quantum system. Following the laws of quantum mechanics, the qubits are subject to superposition and entanglement, which in turn means that they live in a much more complex space than traditional bits and are not restricted to binary outputs, allowing for a more diverse exploration of the solution space for generative modelling applications. A class of such quantum algorithms is parameterized quantum circuits (PQC)<sup>47</sup>, where the qubits are subjected to quantum operations (gates) which are parameterized by real numbers (rotation angles) and arranged in a circuit of consecutive operations. The final quantum state is then measured and the output measurement are collected and statistically create the final outcome. A classical training procedure allows to optimize these rotation angles which the trainable parameters of the quantum network formed by this PQC. In our pipeline the generator will be a quantum network that will be trained on an ideal (noiseless) quantum simulator while the discriminator remains a classical network. The generator outputs are latent vectors in the same latent space as the VAE. To obtain the final generated molecules the generator output is fed back to the decoder part of the VAE.

Our analysis consists of the following steps:

1. Train the VAE and optimize the VAE hyperparameters;
2. Use the encoder part of the VAE to transform the input dataset into input latent vectors, train the GAN with these input latent vectors;
3. Optimize the latent classical GAN hyperparameters relevant for the discriminator; the classical generator is already optimized and follows the MOSES benchmark suite;
4. Replace the classical generator by a quantum generator, train and optimize;
5. Use the decoder and an RDKit validation to produce final generated molecule samples; Perform a comparison between classical and quantum GAN performances with a set of metrics (see below), perform inference on a real quantum hardware.

We present a compact representation of the proposed drug-design pipeline in Figure 1. In our benchmark against classical drug-design pipeline, the quantum generator depicted in red is replaced by a classical generator with a structure following that of the latent GAN from the MOSES benchmark suite. We have used `Torch v2.8.0`<sup>48</sup> and `PennyLane v0.42.3`<sup>49</sup> to implement our pipeline ran on an NVIDIA A100 GPU with 40GB of memory.

### 2.2.1 VAE and latent dimension

The architecture of the VAE, taken over from the MOSES benchmark suite together with default parameter settings, uses Gated Recurrent Units (GRUs) as building blocks. The encoder is made of one bidirectional GRU ( $n_l = 1$ ) with a hidden dimension  $D_h = 256$ , followed by two linear output layers transforming the output vector of the GRU to a vector of the latent space. The decoder is made of three layers of GRU ( $n_l = 3$ ) with hidden dimensions  $D_h = 512$ , each layer (except the last one) followed by a dropout layer. The default dropout probability out of MOSES benchmark suite is zero (hence no dropout layer in practice), but we will later explore the impact of non-zero dropout probabilities.

The SMILES string is tokenized, such that each character of the string is associated to an integer ID, which in turn is embedded as a vector (initially a one-hot vector, but the embedding is also part of the training of the VAE to increase efficiency) according to the SMILES vocabulary table, the dimension of that vector corresponding to the number of characters in the vocabulary table. As such, the GRU processes the input as a sequential data  $x_t$  where each element of the sequence is a vector representing the embedded token ID. The variable  $t$  indexes the character ID positioning in the SMILES string from left to right, equivalent to a temporal index. At a given step  $t$ , a GRU uses two gates to update the internal hidden state  $h_t$ : the reset gate  $r_t$  and the update gate  $z_t$ . The hidden state  $h_t$  is thus computed from the

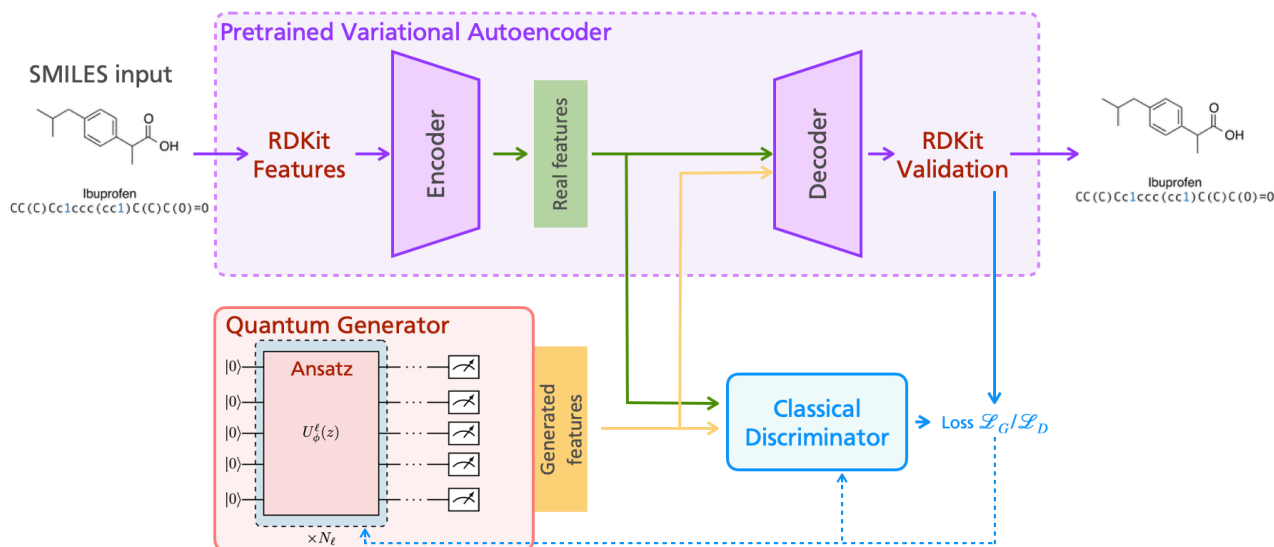


**Figure 1.** Schematic representation of the quantum-augmented drug-design pipeline. The model comprises a pre-trained VAE on the MOSES dataset using SMILES input (in purple), that embeds the original molecules into a low-dimensional latent space, and a quantum GAN with a quantum generator (in red) and a classical discriminator (in blue). The features extracted by the VAE from the input dataset are used for the training of the GAN. The final generated SMILES molecules are reconstructed by inversely transforming the features generated by the quantum generator using the pre-trained decoder of the VAE, and finally validated using RDKit.

hidden state  $h_{t-1}$  and the new candidate hidden state  $n_t$  as follows:

$$\begin{aligned}
 r_t &= \sigma(W_r x_t + U_r h_{t-1} + b_r), \\
 z_t &= \sigma(W_z x_t + U_z h_{t-1} + b_z), \\
 n_t &= \tanh\left(W_n x_t + b_n + r_t \odot (U_n h_{t-1} + b_{n,u})\right), \\
 h_t &= (1 - z_t) \odot n_t + z_t \odot h_{t-1},
 \end{aligned} \tag{1}$$

where the function  $\sigma$  is the sigmoid function controlling the gating mechanism and  $\odot$  stands for Hadamard product (or element-wise product). As a slight abuse of notations, both  $\tanh$  and  $\sigma$  functions are meant to be applied element-wise on each element of the vector argument of these functions. The matrices  $W_{r/t/n}$  and  $U_{r/t/n}$  are the input trainable weights and recurrent trainable weights for the reset gate, the update gate, and the candidate hidden state, respectively. The vectors  $b_{r/z/n}$  and  $b_{n,u}$  are the associated trainable biases for each gate. Note that for the first letter (equivalent to  $t = 0$ )  $h_{t-1}$  corresponds to the initial hidden state at time  $t = 0$ .

For a bidirectional GRU, the sequence  $(x_t)$  is processed in both forward and backward directions, producing a final state which has doubled dimension,  $h_{GRU}^{bi} = (h^{\rightarrow}, h^{\leftarrow})$ . At each step the output is a concatenation of the forward direction (processing the SMILES string from left to right) and the backward direction (processing the SMILES string for right to left). It is important for the encoder of the VAE as it captures information from both past and future contexts in the SMILES string, in turn allowing for a richer and more accurate encoding of the SMILES sequence. When there are more than one layer in the GRU, the input of layer  $l$  is the final hidden state (output) of layer  $(l - 1)$ ,  $h_t^{(l-1)}$ . When a dropout layer is

included, the actual input of layer  $l$  is a modification of  $h_t^{(l-1)}$  into  $\delta_t^{(l-1)} h_t^{(l-1)}$  where  $\delta_t^{(l-1)}$  is a Bernoulli random variable equal to zero with a probability equal to dropout.

The dimensionality of the latent space is a key parameter of the pipeline. The output of the generator, both for the classical and quantum GANs, has to match the dimension of the latent space. For the quantum generator there is a linear correspondence between the number of qubits used in the quantum circuit and the latent dimension  $D_l$ : either a one-to-one correspondence or a one-to-two, depending on how the measurements outcome from the quantum network is collected, see the next sections.

As current quantum computers are still limited in the number of qubits, and as the simulation of quantum states with classical resources is exponentially costly, our default setup for latent space is a latent dimension of 10, hence using at most 10 qubits. We have studied a latent dimension up to 30 and validated our pipeline by performing the training on noiseless quantum simulators using classical resources. We have also performed an inference on a superconducting-qubit hardware, the `ibm_kingston` computer with 156 qubits on an IBM Heron chip.

## 2.2.2 Classical and hybrid quantum GAN architecture

The heart of our pipeline is the GAN architecture. Let us define the generator as  $G$  and the discriminator as  $D$ . The training of the adversarial minmax game of the GAN uses the Earth-Mover (or Wasserstein) distance, together with gradient penalty (WGAN-GP), to ensure an efficient mitigation of the effect of mode collapse<sup>33</sup>. The training of the WGAN-GP follows from

$$\min_G \max_D \mathcal{L}_{WGAN}(G, D) + \lambda \mathbb{E}_{\hat{\mathbf{x}} \sim p(\hat{\mathbf{x}})} \left[ \left( \|\nabla_{\hat{\mathbf{x}}} D(\hat{\mathbf{x}})\|_2 - 1 \right)^2 \right], \quad (2)$$

where  $\hat{\mathbf{x}}$  are samples drawn randomly from a uniform distribution  $p(\hat{\mathbf{x}})$ , along straight lines between pairs of points sampled from the input data distribution and the distribution of the generated output from the generator  $G$ . We denote the input data distribution as  $p_{\text{data}}$  and  $p(\boldsymbol{\xi})$  the noise distribution which serves as input for the generator  $G$ . The function  $\mathcal{L}_{WGAN}(G, D)$  is the loss function of the original Wasserstein GAN without the gradient penalty, and corresponds to

$$\mathcal{L}_{WGAN}(G, D) = \mathbb{E}_{\boldsymbol{\xi} \sim p(\boldsymbol{\xi})} [D(\mathbf{x} = G(\boldsymbol{\xi}))] - \mathbb{E}_{\mathbf{x} \sim p_{\text{data}}} [D(\mathbf{x})]. \quad (3)$$

The parameter  $\lambda$  controls the impact of the gradient penalty term and is fixed to  $\lambda = 10^{33}$ .

A WGAN-GP can still suffer from training instability, difficulties for generalization, or a lack of robustness, which is reflected by a sensitivity to the initialization of the trainable parameters of the GAN. Our pipeline hence replaces the WGAN-GP by a hybrid quantum WGAN-GP (from now on simply classical GAN and QGAN), where the discriminator is still a classical network but the generator is now a quantum generator described by a PQC. Following previous studies in the context of high-energy physics or high-quality image generation<sup>40,41,43</sup> we adopt a style-based architecture<sup>42</sup> in the quantum generator<sup>40</sup>. It uses a data re-uploading approach where the input random noise for the generator is implemented in all gates of the quantum circuit, and not just in the first gates on each qubit. This approach has been shown to allow for more flexibility and richness of the quantum generation mechanism for images or high-energy physics applications, but has never been attempted for drug design so far.

The classical GAN architecture in our benchmark follows closely the one from MOSES benchmark suite<sup>37</sup> introduced in<sup>39</sup>. The discriminator (same structure for classical and quantum GANs) is made of three linear (dense) layers for which the dimension of each layer follows the sequence [512, 256, 1], all followed by a LeakyReLU activation function with parameter 0.2, except for the last layer. The classical generator is made of five linear layers with the sequence [128, 256, 512, 1024,  $D_l$ ], each followed by a LeakyReLU activation function with parameter 0.2, except for the last layer. In addition, the second, third, and fourth layer use batch normalization.

We will study two different ansätze for the quantum circuit of the quantum generator that are built from layers which can be repeated  $n_l$  times to increase the expressive power of the model. Such layered structures follow the hardware-efficient ansätze paradigm widely used in variational quantum algorithms, including the variational quantum eigensolver and various QGAN studies<sup>25,47,50,51</sup>. In particular, the

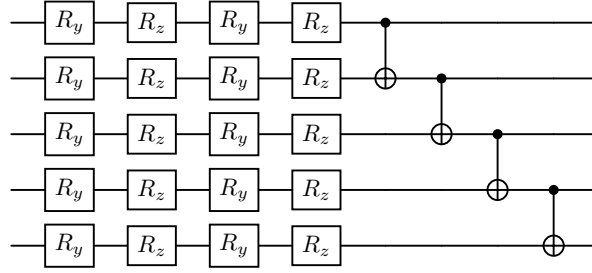


**Figure 2.** Styled simple circuit with five qubits and one layer.

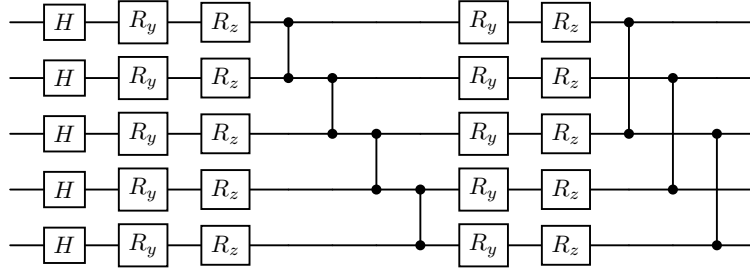


**Figure 3.** Styled basic entangled layer (BEL) circuit with five qubits and one layer. In addition there is a final set of one-qubit  $R_Y$  gates on each qubit to rotate all qubits in the computational basis before performing the final measurement operation.

designs are inspired by parameterized circuit templates available in modern quantum machine-learning frameworks such as PennyLane<sup>49</sup>. The first architecture corresponds to a simple structure composed of single-qubit rotations and controlled rotations arranged in repeated layers (Fig. 2), while the second architecture introduces a basic entangled layer (BEL) (Fig. 3) that enhances correlations between qubits through additional entangling operations<sup>52</sup>. We consider representative circuits with five data qubits. All rotation gates, including the controlled rotation gates, are parameterized by angles in the domain  $[0, 2\pi]$ , defined as

$$\theta_{q,\ell,k} = 2\pi \tanh(\xi_q W_{q\ell k} + b_{q\ell k}), \quad (4)$$

where  $\xi_q$  is the input noise vector element for a given qubit  $q$ ,  $W_{q\ell k}$  is the element of the tensor of trainable parameters, for a given qubit  $q$ , a given layer  $\ell$ , and a given angle label  $k$  corresponding to the  $k$ th rotation gate. The tensor  $\mathbf{b}$  contains the biases. Using the non-linear function  $\tanh()$  helps to avoid over-rotation during the training phase, further mitigating the (quantum) mode collapse.

We construct output vectors from the quantum circuit by performing quantum measurements of Pauli operators, constructing an expectation value of it. We can use either single readout or dual readout. In the former case one Pauli operator (usually chosen as the  $Z$  operator) is measured for each qubit, so that a quantum generator with  $n_{qb}$  qubits produces a latent vector of dimension  $n_{qb}$ . In the latter case, the dual readout, we exploit the non-commutativity of Pauli  $X$  and Pauli  $Z$  operators to use the same quantum circuit but performing two independent measurements for each qubit. The quantum generator with  $n_{qb}$  qubits thus outputs a latent vector of dimension  $2n_{qb}$ , at the expense of running twice as many quantum measurements to obtain the same similar quantum precision of the final outcome compared to single readout.

Because of the exponential cost of simulating quantum circuits, we have restricted ourselves to up to 15 qubits with dual readout in our analysis, corresponding to a maximum latent dimension of 30. We have adopted the latent dimension of 10 as our default setting, with either 10 qubits and single readout or five qubits and dual readout, as used for the quantum inference on `ibm_kingston`. This choice of default latent dimension is driven by the analysis of the classical latent GAN, where a latent dimension greater than 10 does not change significantly the results, see also Table 20 in the supplementary material section. We will also present results on quantum simulator with a latent dimension of 30, with 15 qubits and dual readout.

## 2.3 Metrics

The definitions of the metrics used in this analysis are taken from the MOSES benchmark suite and are standard for drug design. We list them below:

- **Distinct Fraction** ( $\epsilon_d$ ): Calculates fraction of molecules after string de-duplication has been applied to the generated SMILES molecules.
- **Fraction of valid molecules** ( $\epsilon_v$ ): Reports the validity of generated SMILES strings and is defined using RDKit molecular structure parser that checks atom valency and consistency of bonds in aromatic rings.
- **Fraction of unique molecules** ( $\epsilon_u$ ): Checks that the model does not collapse to producing only a few typical molecules.
- **Novelty**: Fraction of the generated molecules that are not present in the training set. Low novelty indicates overfitting.
- **Filters**: is the fraction of generated molecules that pass filters applied during dataset construction. While the generated molecules are often chemically valid, they may contain unwanted fragments that were removed from the training set.
- **Internal diversity (IntDiv)**: Assesses the chemical diversity within the generated set of molecules. This metric detects a common failure case of generative models—mode collapse. With mode collapse, the model produces a limited set of samples, ignoring some regions of chemical space.
- **Molecular weight (Weight)**: Sum of atomic weights in a molecule. In general, it is easier to build viable drugs from lighter molecules.
- **LogP**: Octanol-water partition coefficient, a ratio of a chemical concentration in the octanol phase to its concentration in the aqueous phase of a two-phase octanol/water system. It is a measure of lipophilicity and is defined as the ability of a compound to differentially dissolve in a mixture of water and lipids/organic solvents. Using MOSES tools it is computed with the RDKit Crippen estimator<sup>53</sup>. According to the Lipinski’s rule of 5<sup>54,55</sup>, a typical good value of LogP for (oral) drugs is between 0 and 5. We have constructed an associated metrics,  $\epsilon_{LogP}$ , which is the fraction of molecules in this range.
- **Synthetic Accessibility Score (SA)**: Heuristic estimate of how hard (10) or how easy (1) it is to synthesize a given molecule.
- **Quantitative Estimation of Drug-likeness (QED)**: Real number in the interval  $[0; 1]$ , estimating how likely a molecule is a viable candidate for a drug.

The first six metrics are constrained to the interval  $[0; 1]$ , where the desired value is as close to unity as possible. The last four metrics are reported in two ways: either as the Wasserstein distance (denoted as  $\mathcal{W}$ ) between the test and generated dataset, following the MOSES benchmark suite<sup>37</sup>; or as the mean of the distribution itself, calculated on the generated sample. The latter choice allows for removing any dependency of the results on the test dataset and is the preferred choice in our analysis.

As mentioned in the list above, we have also introduced another metric not present in the MOSES analysis<sup>37</sup>, the fraction  $\epsilon_{LogP}$ . As the MOSES analysis was not necessarily restricted to (human) drug discovery, this new metric helps to quantify how many drug candidates we obtain in our quantum-computer-assisted drug-design pipeline are compatible with typical LogP values encountered in viable drugs. It is important to avoid a chemical compound with too high lipophilicity (which can lead to accumulation in fat tissues and fatal toxic issues, or difficulties to penetrate certain barriers in the body) or too low lipophilicity (the compound cannot bind to the target molecule at all). Small negative values for LogP are typical of drug that can be injected, values between 1.3 and 1.8 are ideal oral candidates, values around 2 are good candidates for targeting the central neural system, for example.

There are three different scenarios where the above-mentioned metrics have been used:

1. **VAE hyperparameter optimization**: The aim is to ensure a good ability to encode/decode the SMILES information into/from the latent dimension. We thus aim to maximize internal diversity. Additionally, to suppress over-training and improve generalization, we aim to minimize  $\mathcal{W}(\text{LogP})$ ,  $\mathcal{W}(\text{Weight})$ ,  $\mathcal{W}(\text{SA})$ , and  $\mathcal{W}(\text{QED})$ .

- GAN hyperparameter optimization:** The aim is to improve stability of the training. For the scope of this analysis, only the ratio of training frequency between the generator and discriminator within a given epoch has been changed.
- Classical and quantum GAN performance comparison:** The aim is to compare performance independently of the training or test samples as well as to maximize the chance for generating truly novel molecules. Therefore, all fractions ( $\epsilon_d$ ,  $\epsilon_v$ ,  $\epsilon_u$ ,  $\epsilon_{LogP}$ , novelty, filters, and internal diversity) have been maximized as well as the mean of the QED distribution, while the means of the SA and molecular weight distributions have been minimized.

In order to test the training robustness (i.e. the sensitivity of the model to the initialization of the training parameters), each model has been trained five times with each time a different random seed, so that the quoted values are the mean and standard deviation over these five runs.

In order to assess globally the performance of the quantum GAN models against the classical GAN, we have also used as a final metric the  $Z_0$  significance defined as:

$$Z_0 = \sum_m Z_0^m = \sum_m \frac{\Delta^m}{\sqrt{(\sigma_1^m)^2 + (\sigma_2^m)^2}}, \quad (5)$$

where the sum runs over all the relevant metrics for scenario comparison as listed in the list above (fractions  $\epsilon_d$ ,  $\epsilon_v$ ,  $\epsilon_u$ ,  $\epsilon_{LogP}$ ; novelty; filters; internal diversity;  $\langle QED \rangle$ ;  $\langle SA \rangle$ ;  $\langle Weight \rangle$ ) and  $\Delta$  is the difference between the means of the respective metric  $m$ . The quantities  $\sigma_1^m$  and  $\sigma_2^m$  in Equation 5 refer to the standard deviations of the metric  $m$  for the reference scenario and for the scenario under study, respectively. The construction  $\Delta$  depends of whether the metric  $m$  is aimed to be maximized or minimized. In the former case, such as for efficiencies,  $\Delta^m = \mu_2^m - \mu_1^m$  where  $\mu_1^m$  and  $\mu_2^m$  refer to the means of the metric  $m$  for the reference scenario and for the scenario under study, respectively. In the later case, such as for the SA or Weight,  $\mu_1^m$  and  $\mu_2^m$  are swapped,  $\Delta^m = \mu_1^m - \mu_2^m$ . For global significance, we will take the average of  $Z_0$ , hence dividing by the number of metrics used in the comparison. The ground truth in this calculation is the classical GAN result taken as the benchmark reference point. The sign of the significance then indicates improvement or degradation of the quantum GAN designs over the classical GAN. To guide the reader, we remind  $|\langle Z_0 \rangle| < 1$  indicates globally a performance which is comparable between classical and quantum pipelines (the variance is less than  $1\sigma$ ), while values above indicate sizable improvement or sizable degradation. More details with an example are presented in Section 2.4.2.

We present in the supplementary material more details on the metrics applied to the input distributions, see Section 1 of the supplementary material. For more details on the sensitivity of the metrics to the number of generated samples, see Section 3.

## 2.4 Training details

### 2.4.1 Training of the VAE

The VAE has been trained following the procedure in the MOSES benchmark suite<sup>37</sup>. This means in particular that we have used a batch size of 64 and a gradient clipping threshold of 50. We have used Adam optimizer<sup>56</sup> with a nominal learning rate equal to  $3 \times 10^{-4}$ . The study of the loss function for training and validation datasets has indicated that  $N_{ep} = 1,000$  epochs produce an optimal result.

We have performed a small hyperparameter tuning of the VAE by varying the parameters listed in Table 1. The learning rate is fixed at  $3 \times 10^{-4}$  in the nominal setup, we explore also a learning-rate scheduling for which the tuned parameter is a cosine schedule starting from  $10^{-3}$  and ending at  $10^{-5}$  for the final training epochs. We provide the tuned values of these parameters, leading to the metrics comparison presented in Table 2. The comparison of the various metrics distributions between the nominal and the tuned VAE is presented in Figure 4. We provide more details on the VAE training results in the supplementary material, Section 2 of the supplementary material.

Overall, the performance of all VAE training runs is very good and consistent: The metric comparison shows an improvement for the tuned VAE, however modest. We have also performed an additional test of the robustness of the decoder of the VAE, to ensure that it can efficiently decode the latent space since this is how we obtain the final generated molecules. This means we have to make sure that the decoder does

Metrics	Nominal VAE	Tuned VAE
Learning rate (lr)	$3 \times 10^{-4}$	Scheduled $10^{-3} \rightarrow 10^{-5}$
Encoder $n_l$	1	1
Encoder $D_h$	256	512
Decoder $n_l$	3	4
Decoder $D_h$	512	512
Decoder dropout	0	0.75

**Table 1.** VAE hyperparameter settings comparison between nominal (MOSES default) and tuned settings.

Metrics	Train set	Nominal VAE	Tuned VAE
IntDiv	0.898	0.896	0.896
$\mathcal{W}(\text{LogP})$	0.091	0.087	0.079
$\mathcal{W}(\text{SA})$	0.268	0.275	0.251
$\mathcal{W}(\text{QED})$	0.027	0.025	0.022
$\mathcal{W}(\text{Weight})$	42.8	43.9	41.8
$N_{\text{params}}$	–	4,271,250	6,472,082

**Table 2.** Metrics derived from the training set and sets generated by the nominal and tuned VAE. Internal diversity is computed as the mean over the respective samples, whereas the remaining four metrics are the average Wasserstein distances between the sample in question and the test sample for the corresponding metric.

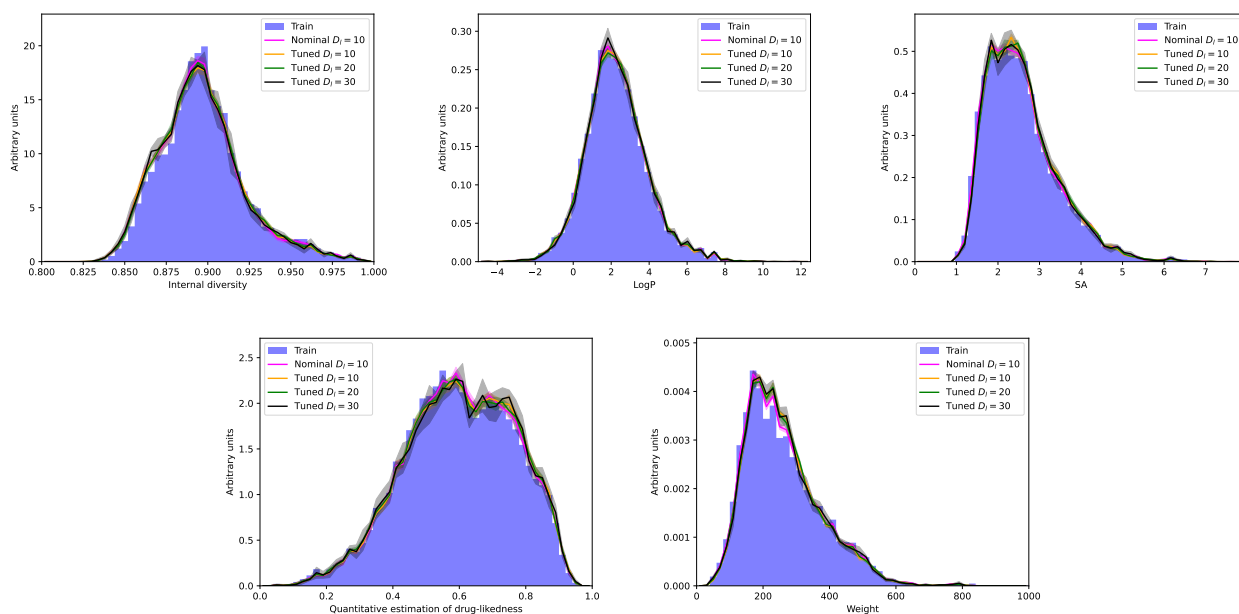


**Figure 4.** Distributions of metrics derived from the input train set and the generated sets using the nominal and tuned VAE decoder.

not collapse the latent space back to a small subset of the molecular space. A shape study of the decoder has been performed and demonstrates that it is sensitive to the shape of the latent vector distribution, confirming that the VAE does not collapse to a contrived subspace of the molecular input space. For more details, see Section 5 of the supplementary material.

## 2.4.2 Latent GAN

The latent QGAN is trained on a noiseless quantum simulator (state-vector simulation) and the final generated molecules are filtered with RDKit to check that they are chemically valid. We will also perform an experimental sampling on a quantum hardware, the IBM `ibm_kingston` system based on the Heron quantum chip.

The training of both classical and quantum latent GANs follows from the loss function described in Equations 2 and 3 using again the Adam optimizer. For the classical GAN, the nominal learning rate is  $2 \times 10^{-4}$  with Adam parameters  $\beta_1 = 0.5$  and  $\beta_2 = 0.9$ . The number of epochs has been set to  $N_{ep} = 100$ , and the ratio of the discriminator to generator training frequency was changed from five (default in MOSES benchmark suite) to one (further denoted as “tuned GAN”). The loss functions for the nominal and tuned GANs over a number of epochs are presented in Figure 5.

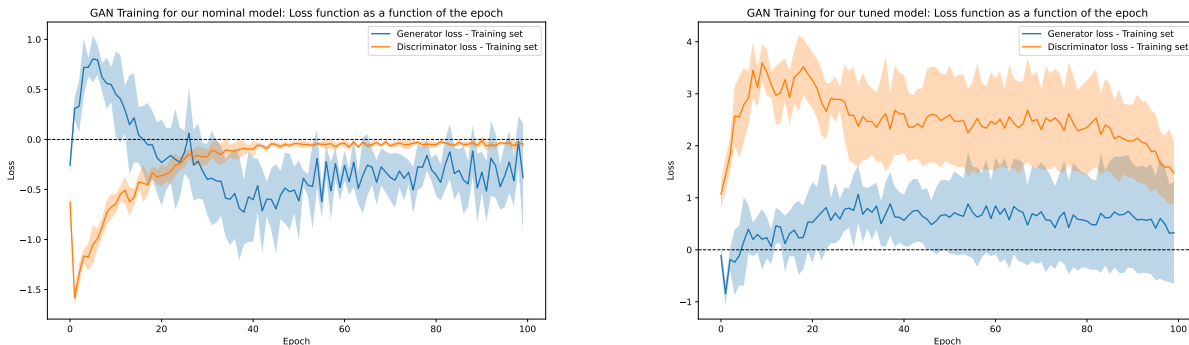


**Figure 5.** Comparison of the loss functions for the nominal (left) and tuned (right) GANs. Each model was run with five different seeds, the shaded band denotes a  $\pm 1\sigma$  deviation.

Metrics	Train set	Tuned VAE	Nominal GAN	Tuned GAN
$\epsilon_d$	0.982	$0.605 \pm 0.017$	$0.510 \pm 0.007$	$0.481 \pm 0.030$
$\epsilon_v$	1.000	$0.868 \pm 0.006$	$0.911 \pm 0.006$	$0.917 \pm 0.012$
$\epsilon_u$	1.000	$0.993 \pm 0.001$	$0.986 \pm 0.002$	$0.986 \pm 0.003$
Novelty	0.000	$0.461 \pm 0.026$	$0.501 \pm 0.015$	$0.536 \pm 0.015$
Filters	0.734	$0.728 \pm 0.002$	$0.723 \pm 0.003$	$0.721 \pm 0.011$
IntDiv	0.898	$0.896 \pm 0.000$	$0.902 \pm 0.002$	$0.898 \pm 0.004$
$\mathcal{W}(\text{LogP})$	0.091	$0.078 \pm 0.004$	$0.291 \pm 0.026$	$0.354 \pm 0.037$
$\mathcal{W}(\text{SA})$	0.268	$0.249 \pm 0.004$	$0.375 \pm 0.028$	$0.437 \pm 0.080$
$\mathcal{W}(\text{QED})$	0.027	$0.023 \pm 0.001$	$0.039 \pm 0.003$	$0.038 \pm 0.005$
$\mathcal{W}(\text{Weight})$	42.8	$42.4 \pm 1.0$	$93.0 \pm 4.6$	$99.4 \pm 10.6$
$\epsilon_{\text{LogP}}$	0.883	$0.886 \pm 0.003$	$0.895 \pm 0.002$	$0.898 \pm 0.006$
$\langle \text{SA} \rangle$	2.561	$2.579 \pm 0.004$	$2.454 \pm 0.028$	$2.391 \pm 0.080$
$\langle \text{QED} \rangle$	0.596	$0.604 \pm 0.001$	$0.592 \pm 0.006$	$0.599 \pm 0.007$
$\langle \text{Weight} \rangle$	261.5	$260.5 \pm 1.1$	$210.3 \pm 4.6$	$203.9 \pm 10.6$
$\langle Z_0 \rangle$	–	Reference	+1.45	+0.86

**Table 3.** Metrics results for the VAE and classical GANs. All GANs use the tuned VAE for the latent space representation. Unlike the other cases, the nominal GAN uses the nominal GAN hyperparameter settings as discussed in the text. The quoted standard deviation comes from running each scenario five times with different seeds for the initialization of the trainable parameters.

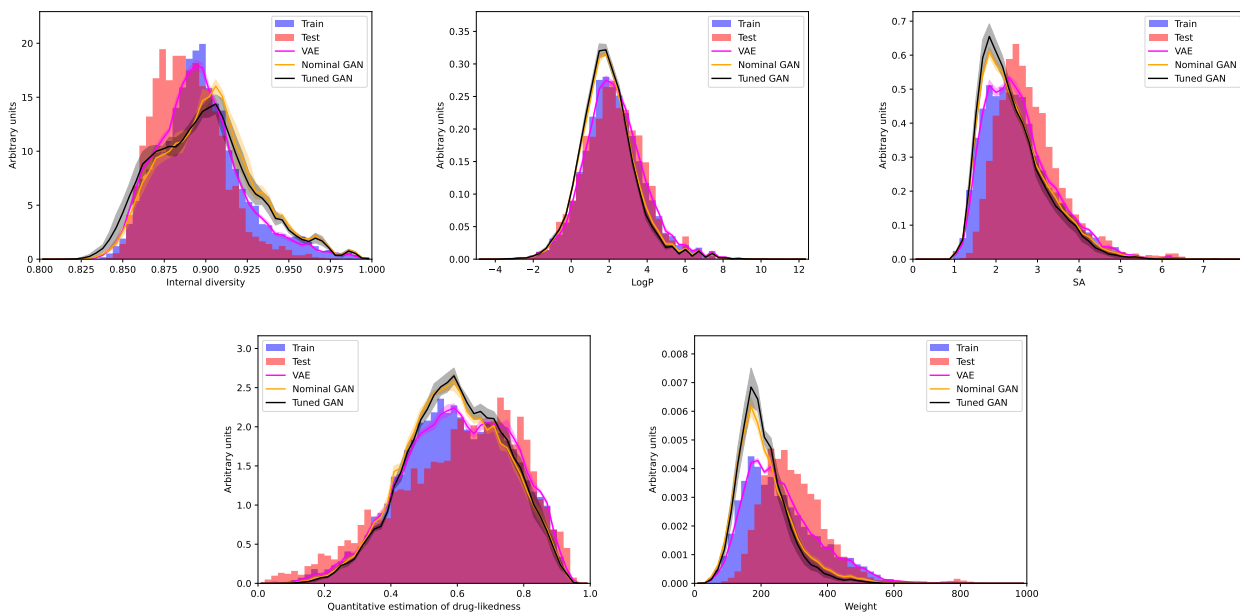


**Figure 6.** Comparison of the metrics for the models used in the analysis. For the VAE, the tuned version is used, for the GAN, not only the tuned VAE is used but also the GAN is tuned itself. Each model was run with five different seeds, the shaded band is defined as  $\pm 1\sigma$  deviation.

We present in Table 3 the metrics estimated from the samples generated by the respective models. The table is split into four parts:

1. The first six metrics are interpretable as efficiencies – distributions between 0 and 1 estimated from the distributions themselves, where the closer to unity, the better.
2. The second part, denoted with  $\mathcal{W}(X)$ , presents the Wasserstein distances between the test sample and the generated sample for a variable  $X$  defined by the MOSES analysis.
3. The third part presents the fraction of the samples with  $|\text{Log}P| < 5$  and mean values of the distributions of the Synthetic Accessibility Score (SA), Quantitative Estimation of Drug-likeness (QED), and molecular weight.
4. The last part then presents a performance comparison of scenarios by summing the individual statistical compatibilities of metrics from parts one and three.

As discussed in Section 2.3, in a situation where the task is to evaluate whether a model is producing novel and unknown molecules with desired properties, maximizing the Wasserstein distance from the test sample should be a good objective. Such an approach poses a subtle yet important problem: If the model produces molecules with metrics distribution distant from the test set but similar to the training set, it may incorrectly prefer reproducing the training set.

This is exemplified in Figure 6, comparing training and test input samples with samples generated by the VAE decoder, the nominal GAN, and the tuned GAN models. In all cases, the optimized VAE hyperparameter settings were used. Across all distributions, the GAN exhibits greater capacity to generate samples farther from the training and test datasets, confirming the observation made in<sup>37</sup>. However, it is also visible that all distributions tend to be close to the training set. If there were a model positioned in the opposite direction from the test sample relative to the training sample, but closer to the test sample, maximizing the Wasserstein distance would still prefer the model that reproduces the training dataset. The maximization procedure would lead to an incorrect conclusion. For that reason it has been decided to use only the seven fractions ( $\epsilon_d$ ,  $\epsilon_v$ ,  $\epsilon_u$ , Novelty, Internal diversity, Filters and  $\epsilon_{\text{Log}P}$ ) and mean of the SA, QED and Weight distributions for the construction of our single scalar average  $\langle Z_0 \rangle$  significance as a metric for scenario comparison.

Finally, the  $\langle Z_0 \rangle$  significance difference in Table 3 shows that both GANs are performing better than the VAE which is in agreement with the intuition we get from the plots.

### 3 RESULTS

In this section we present the comparison of performance of the classical and quantum GANs. In addition to the metrics discussed in Section 2.3, we also compare the parameter counts and training stability of the quantum model with those of a classical counterpart.

As explained in Section 2.2.1 we present quantum training with a maximum latent dimension of 30, corresponding to quantum circuits with 15 qubits and dual readout. We start with our default scenario with a latent dimension of 10 in Section 3.1, we present a comparison between the different quantum scenarios with up to latent dimension of 30 in Section 3.2, and present the results of our quantum inference on the IBM quantum computer `ibm_kingston` in Section 3.3.

#### 3.1 Classical vs quantum GANs

The default scenario we investigated was using the latent dimension 10, tuned VAE, and classical GAN hyperparameters. The two quantum circuits described in Section 2.2.2 are compared in the nominal setup of five qubits, two layers, and dual readout. The quantum GANs are trained with 100 epochs. Figure 7 presents the loss function on the training set for the BEL quantum generator for the nominal (left) and tuned (right) GAN training parameters. Compared to Figure 5 it is clear that the loss function has a much smoother trend and fewer variations. The QGAN in our pipeline leads to a more robust pipeline compared to the baseline with latent classical GAN.

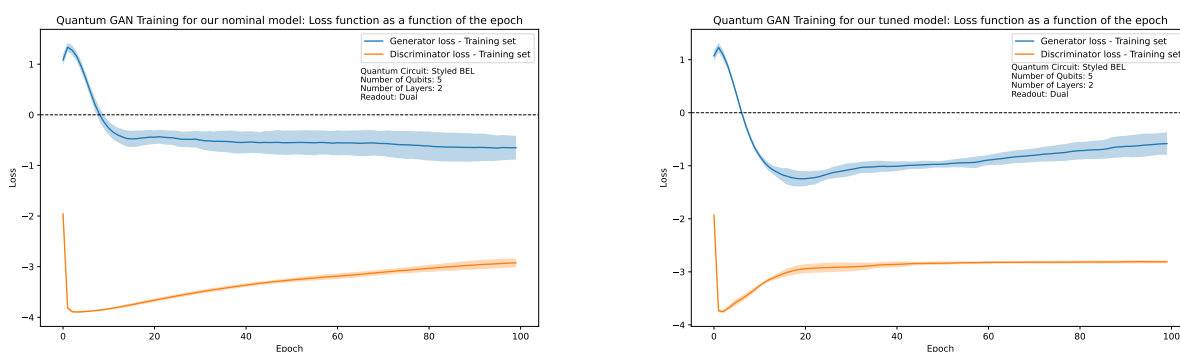


**Figure 7.** Comparison of the loss functions for the nominal (left) and tuned (right) quantum GANs with the BEL circuit. Each model was run with five different seeds, the shaded band is defined as  $\pm 1\sigma$  deviation.

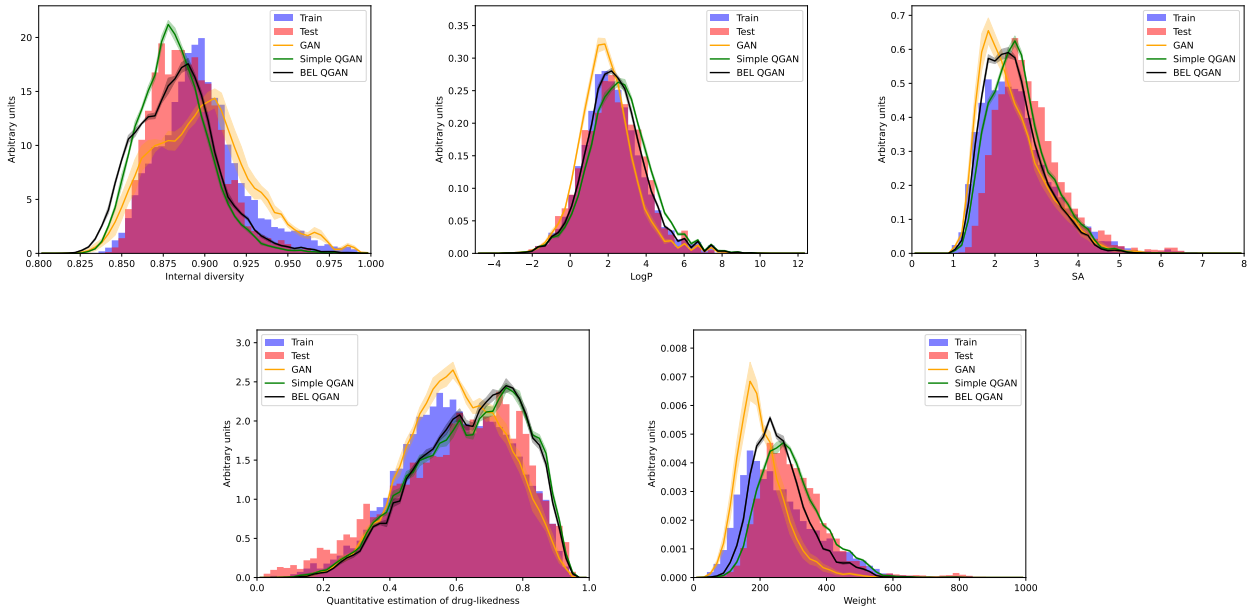
Table 4 presents the metrics comparison for the nominal circuit setting for the QGANs and the classical GAN. It is worth mentioning that results of the quantum circuits are compatible with the classical GAN within one standard deviation. As expected, the simple circuit performs worse than the BEL circuit. The results of the classical GAN were obtained with more than 6,400 times more parameters than the results of the BEL QGAN.

Figure 8 presents the comparison of the metrics distributions for the classical GAN and two QGANs. The classical and quantum GANs exhibit distinct shapes beyond their respective uncertainty bands. There is also a difference between the simple and BEL circuits. For the distributions of internal diversity and molecular weight, the classical GAN tends to have the distribution skewed towards desirable values – unity for internal diversity and zero for the weight. However, QGANs show a higher likelihood of the molecule being a viable drug (QED).

Figure 9 presents the distributions of the 10 latent vectors for the train, test, classical and quantum GANs. The QGAN uses the BEL circuit with nominal setting of five qubits, two layers and dual readout. When constructing the latent vectors, the VAE encoder adds a random noise term, so even the train and

Metrics	Tuned GAN	Simple QGAN	BEL QGAN
$N_{params}$	705,162	20	110
$\epsilon_d$	$0.481 \pm 0.031$	$0.529 \pm 0.003$	$0.523 \pm 0.003$
$\epsilon_v$	$0.917 \pm 0.012$	$0.831 \pm 0.002$	$0.875 \pm 0.003$
$\epsilon_u$	$0.986 \pm 0.003$	$0.994 \pm 0.000$	$0.993 \pm 0.001$
Novelty	$0.536 \pm 0.015$	$0.572 \pm 0.003$	$0.548 \pm 0.003$
IntDiv	$0.898 \pm 0.004$	$0.882 \pm 0.000$	$0.883 \pm 0.000$
Filters	$0.721 \pm 0.011$	$0.737 \pm 0.003$	$0.719 \pm 0.002$
$\epsilon_{LogP}$	$0.898 \pm 0.007$	$0.883 \pm 0.001$	$0.896 \pm 0.002$
$\langle SA \rangle$	$2.391 \pm 0.076$	$2.575 \pm 0.007$	$2.448 \pm 0.007$
$\langle QED \rangle$	$0.599 \pm 0.007$	$0.641 \pm 0.001$	$0.643 \pm 0.001$
$\langle Weight \rangle$	$203.9 \pm 10.6$	$294.8 \pm 0.8$	$261.4 \pm 0.8$
$\langle Z_0 \rangle$	Reference	-1.00	-0.26

**Table 4.** Comparison of the performance of the two types of quantum GANs with respect to the classical GAN. All models use tuned VAE and GAN training parameters. The quantum circuit use five qubits, two layers and dual readout to produce a latent vector of dimension 10.



**Figure 8.** Comparison of the metrics for the two quantum circuits and the classical GAN. All models use tuned VAE and GAN training parameters. The quantum circuit uses five qubits, two layers and dual readout to produce a latent vector of dimension 10. Each model was run with five different seeds and the shaded band is defined as  $\pm 1\sigma$  deviation.

test samples with fixed inputs, when run five times, produce slightly different distributions and hence the uncertainty band even for those scenarios. All but vectors six and seven show no difference between any of the four samples. For more details on the correlations between the latent vectors, see Section 6.

### 3.2 Scenario comparison

As mentioned in previous sections, the highest achievable latent dimension is 30, because anything beyond 15 qubits is too computationally complex for the hardware used in this analysis. Taking these limitations into account, a comprehensive study of various scenarios has been performed and presented in Table 5.

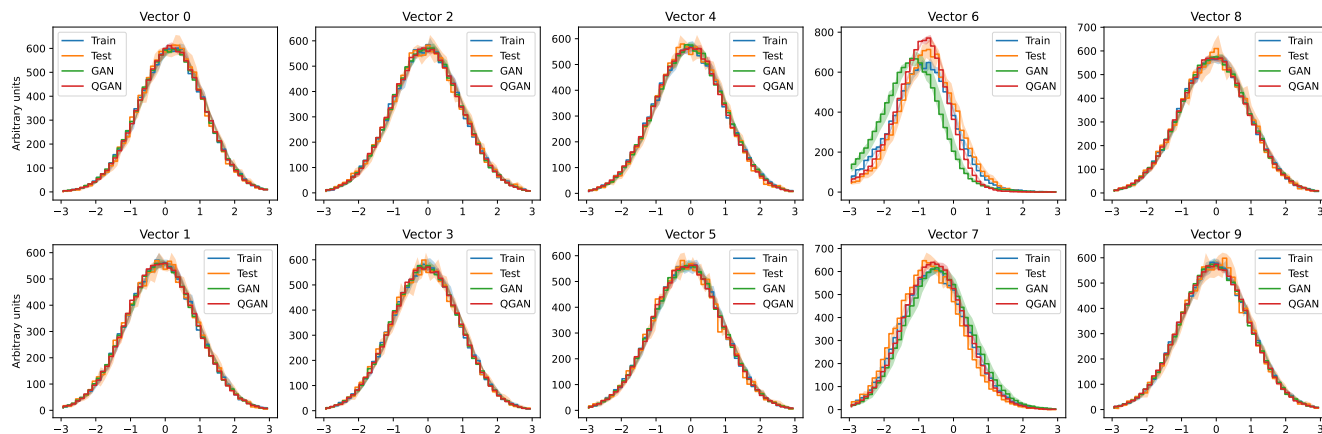


**Figure 9.** Distribution of latent vectors for the train, test, classical GAN and BEL QGAN samples.

The scenario comparison is based on the aggregated  $Z_0$  significance estimated for metrics as described in Section 2.3. As baseline, the classical GAN with optimized training hyperparameters and the VAE pipeline with a latent dimension of 10 has been selected. All scenarios are within one standard deviation, hence statistically compatible. Any additional difference is therefore minor from a statistical perspective, nevertheless there are some statements we can make.

- Increasing the size of the latent dimension does not seem to improve the performance of the scenario even for the classical GANs.
- For the simple circuit the improvement due to single readout (higher number of qubits) is smaller than for the BEL circuit. This is likely connected to the complexity of the circuit.
- The number of QGAN layers does not seem to have any impact on the result.
- For dual readout and a latent dimension of 20, the difference between the QGAN and the classical GAN (with the same latent dimension) seems to be much smaller than for a latent dimension of 10.
- For dual readout and a latent dimension of 30, the difference between the QGAN and the classical GAN (with the same latent dimension) seems to be much smaller than for a latent dimension of 10 even if there is larger difference than for a latent dimension of 20.
- The BEL circuit seems to have the same performance for latent dimensions of 20 and 30 (i.e. 10 and 15 qubits).
- The only consistent improvement in QGAN performance for a given latent dimension is going from dual to single readout. We have restricted our analysis in the single readout case to a latent dimension of 10 as otherwise we would need significantly more computing power for latent dimensions of 20 or 30 and single readout, without a clear hint of improvement with the dataset we have investigated.

More details can be found in the supplementary material, see Section 7 of the supplementary material.

### 3.3 Inference runs on quantum hardware

To validate the ability of the QGAN to generate new molecules using actual quantum hardware, we have performed the sampling of 2,500 molecules on the `ibm_kingston` quantum system provided by IBM, using the model of the QGAN with five qubits, two layers, and dual readout trained on a noiseless quantum simulator. To assess the performance of the quantum device and evaluate the effect of quantum noise, we have also generated 2,500 molecules sampled on quantum simulator, as well as 2,500 samples obtained by the classical generator from the classical GAN. This choice of a lower sample compared to the default choice of 30,000 molecules is driven by cost consideration and time spent on the quantum device. It should be noted that this is already a sufficiently large sample to draw meaningful conclusions.

In contrast with noiseless quantum simulations using state-vector simulation, hence infinite precision on the quantum state, we have to select the number of measurements performed on the quantum computer to collect the expectation values. We have performed our experiment with 1,000 shots and used the batch

Latent Dimension ( $N_{params}$ )	GAN	Readout	$n_{qb}$	Simple QGAN		BEL QGAN		
				$n_l = 2$ ( $n_{par}$ )	$n_l = 4$ ( $n_{par}$ )	$n_l = 2$ ( $n_{par}$ )	$n_l = 4$ ( $n_{par}$ )	$n_l = 6$ ( $n_{par}$ )
10 (705,162)	Reference	Dual	5	-1.00 (20)	-1.01 (40)	-0.26 (110)	-0.27 (210)	
		Single	10	-0.84 (40)	-0.83 (80)	-0.10 (220)	-0.08 (420)	-0.11 (620)
20 (716,692)	-0.25	Dual	10	-0.28 (40)		-0.32 (220)		
30 (728,222)	-0.26	Dual	15	-0.39 (60)		-0.32 (330)		

**Table 5.** Average  $\langle Z_0 \rangle$  comparison of different scenarios between classical GANs and QGANs using different setup for the QGANs. The numbers in parenthesis in the first column are the number of trainable parameters and reflect the model capacity (i.e. complexity).

mode on IBM Cloud. When going on the real quantum hardware, the quantum circuit we have designed need to be adapted to the actual device topology and to the set of gates available on this device: This is the transpilation step. For our calculation on the `ibm_kingston` device we have used default qiskit runtime parameters for the transpilation method (optimization = 2) and the resilience level (resilience = 0, no error mitigation applied).

Table 6 presents the comparison of metrics between the classical GAN and the QGAN with BEL circuit and nominal settings ( $n_{qb} = 5$ ,  $n_l = 2$  and dual readout). Despite the somewhat limited statistics, the inference of the quantum hardware delivers similar results when compared to using the noiseless quantum simulator. Running on current noisy intermediate-scale quantum computers does not degrade significantly the performance of our pipeline. In fact, most of the metrics are slightly better for the IBM QGAN than for the ideal QGAN, but it should be noted that for this comparison we have not performed an inference with five different initializations of the trainable parameters. We do not expect that performing these five different runs would have significantly impacted the observations drawn in this section, however this would have been quite expensive to run five times our experiment on the quantum computer.

Comparing the results obtained with our QGAN pipeline with the result from the classical GAN with an identical number of generated samples, a similar comparison as performed in Section 3.1 for the training performance, a reasonable consistency between the sets of results is observed. This statement is also supported by Figure 10 which displays the distribution of metrics, comparing the three GAN scenarios: classical GAN in purple, noiseless QGAN simulation in red, and QGAN ran on `ibm_kingston` in black.

For illustration, Figure 11 presents a subset of molecules generated on the `ibm_kingston` quantum computer. These molecules were not present in the dataset (training and validation), demonstrating the ability of the QGAN to create new molecules on the quantum hardware in the inference step.

## 4 DISCUSSION AND OUTLOOK

In this work, we have adapted the MOSES framework for quantum-assisted drug design, using a latent style-based Wasserstein GAN where the generator is replaced by a quantum network. The underlying VAE, encoding the molecules in the latent space in which the QGAN operates, has been optimized to the dataset we have used for benchmarking our proposed new pipeline against existing

Metrics	Classical GAN	QGAN (noiseless)	QGAN (ibm_kingston)
$\epsilon_d$	0.689	0.892	0.892
$\epsilon_v$	0.947	0.934	0.955
$\epsilon_u$	0.990	1.000	1.000
Novelty	0.310	0.338	0.336
IntDiv	0.915	0.881	0.890
Filters	0.719	0.706	0.729
$\epsilon_{LogP}$	0.906	0.899	0.915
$\langle SA \rangle$	2.389	2.424	2.305
$\langle QED \rangle$	0.543	0.647	0.621
$\langle \text{Weight} \rangle$	156.2	264.8	209.8

**Table 6.** Metrics comparison calculated with 2,500 generated molecules, between classical GAN, the style QGAN on noiseless simulator, and the style QGAN inference on ibm\_kingston. The quantum generator uses  $n_{qb} = 5$ , a number of layers  $n_l = 2$ , and dual readout.

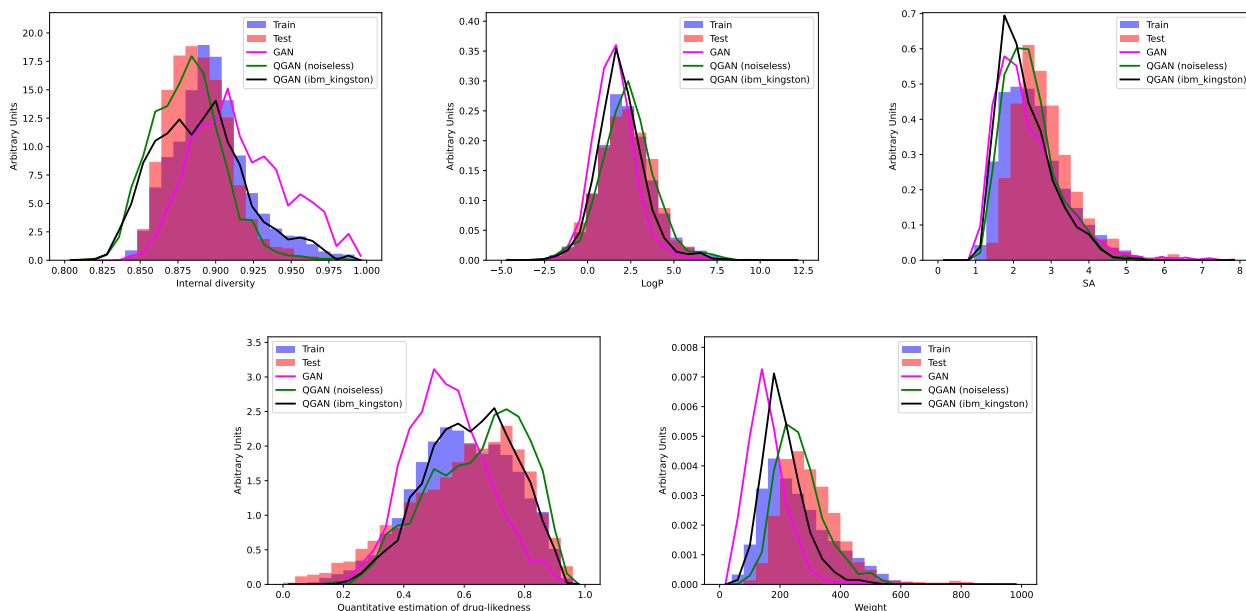


**Figure 10.** Distributions of LogP, SA, and QED metrics for the generation of 2,500 molecule using a classical GAN, the style QGAN ran noiseless simulator, and the style QGAN ran on ibm\_kingston. The quantum generator uses  $n_{qb} = 5$ , a number of layers  $n_l = 2$ , and dual readout.

standard latent classical GAN pipelines as implemented in the MOSES benchmark suite. We have also tuned the classical GAN parameters.

We have presented several innovations compared to the existing pipelines: 1) We have adapted for the first time the style-based approach into a computer-assisted drug design pipeline, leveraging data re-uploading to increase expressivity; 2) We have also used a novel non-linear expression of the rotation angle in the various quantum gates of the two different quantum circuits we have investigated, in order to further prevent quantum mode collapse; 3) We have used a subset of MOSES dataset, which is an industry relevant dataset for machine-learning-assisted bio-molecular studies. After training both classical and quantum GANs on classical computing resources with GPUs, we have performed a performance comparison using various standard metrics relevant for drug design, such as LogP, molecular weight, quantitative estimation of drug-likeness (QED), novelty, uniqueness. Calculating an average  $\langle Z_0 \rangle$  score, we have quantified the statistical performance of the QGAN and found out that our pipeline delivers statistically compatible, competitive performance. For some metrics we even have obtained statistically significantly better results

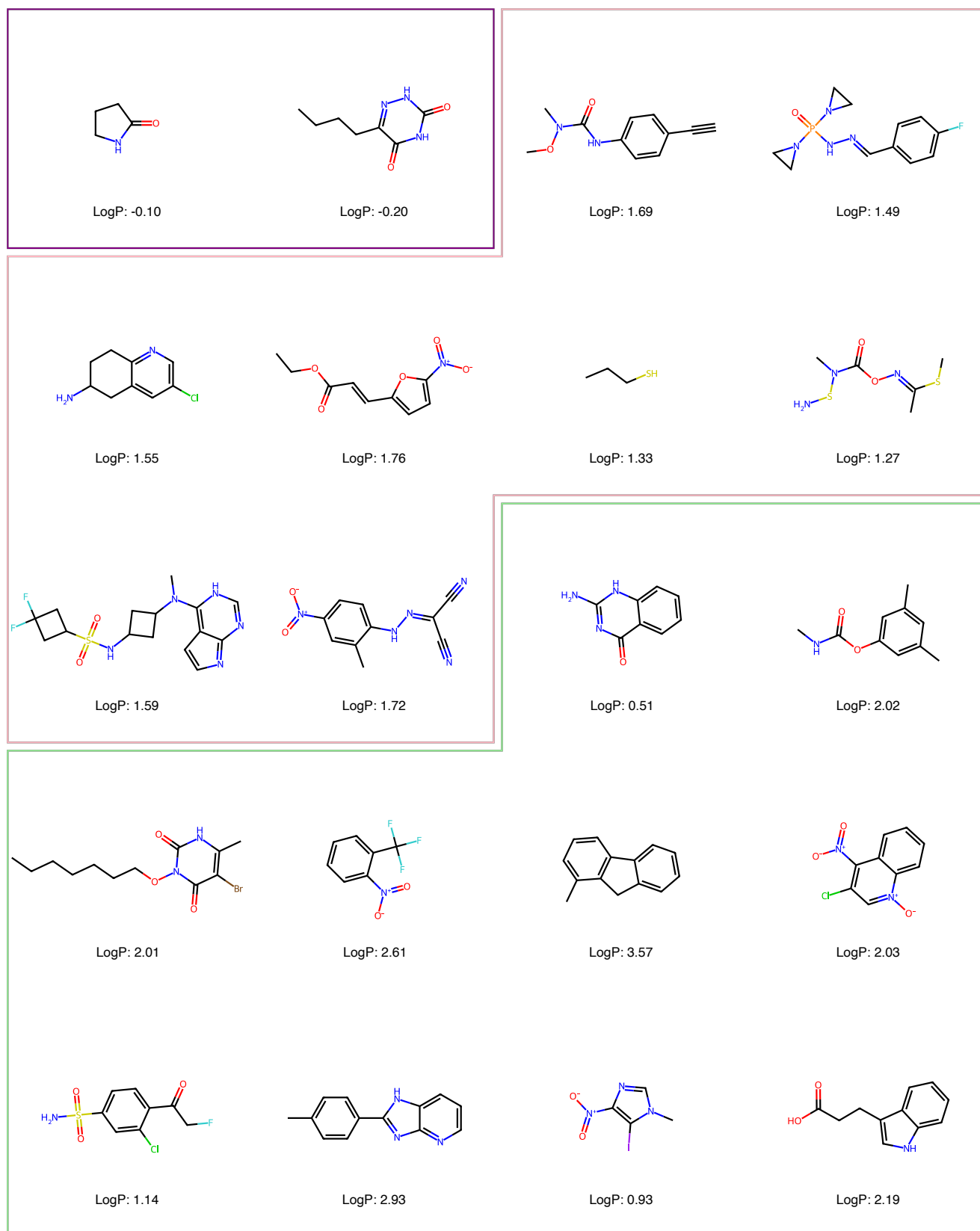


**Figure 11.** Random selection of the 2,500 generated molecules sampled on `ibm_kingston`, passing the RDKit filters and all new compared to both the training and test dataset. The purple cluster contains molecules with LogP values compatible with injectable drugs; the pink cluster contains molecules with LogP values ideal for oral ingestion; the green cluster contains all other molecules with LogP not in the previous categories and still viable drug candidates with  $|\text{LogP}| < 5$ .

with the QGAN, for example average QED or for the fraction of unique molecules produced by the pipeline. In all cases the QGAN pipeline offers a significant improvement: our default QGANs have up to 110 trainable parameters, compared to the 705,162 trainable parameters of the classical GAN pipeline. This massive reduction in the neural network capacity, by a factor of 6,400, is a major improvement towards increased explainability. Compared to previous studies of quantum generative modelling pipelines for drug design, we have been able to obtain competitive results beyond the small-molecule regime. To estimate any potential degradation of the results due to running on real noisy hardware, 2,500 samples have been also generated on a quantum computer, the `ibm_kingston` with 156 qubits on an IBM Heron chip, for the BEL QGAN circuit. The results have been found in good agreement with the results from the ideal noiseless quantum simulator, signaling a robust pipeline with respect to the the expected quantum noise degradation.

There are various directions for future work. The first, immediate extension requires including conditioning in the QGAN pipeline<sup>25</sup>. This would restrict the generation of molecules to specific criteria tailored to e.g. the targeted disease, or to defined toxicity thresholds. The generation mechanism is then enhanced by allowing the (quantum) generator to only sample specific molecules of interest. This can be viewed as type of fine tuning of the generative pipeline. The simplest way to perform this in the current setup is to add ancilla qubits and then entangling them to the measured qubits with trainable controlled rotations. A second direction of high interest is to improve the efficiency of the minmax game between the discriminator and the generator. We have performed several preliminary studies when varying the ratio between discriminator and generator steps in a given training epoch, leading to potentially choosing a ratio of the discriminator to generator training frequency to higher values for the QGAN, different from the tuned choice for the classical GAN. Finally, a very exciting direction of research is investigating hybrid training schemes where both classical resources (GPUs) and quantum resources are used in the training phase. We have so far performed the training entirely on a quantum state-vector simulator running on a GPU. Performing the training in a hybrid mode, with some epochs trained directly on the quantum hardware, would capture the quantum noise characteristics in the model itself which in turn is expected to enhance the quality of the final sampling on the quantum hardware. Along this direction, better training methods or more hardware-training-efficient circuits<sup>57</sup> to perform the entire training efficiently on a quantum hardware should be explored to increase the power of the pipeline and allow for training much wider quantum networks with hundreds of qubits, exploring molecular dataset of high complexity requiring a latent space of dimension 100 or more.

## FUNDING

The author(s) declares that financial support has been received for this work and/or its publication. The work from R. P. has been supported by PricewaterhouseCoopers (PwC).

## REFERENCES

- (1) Wouters, O J McKee, M Luyten, J Estimated Research and Development Investment Needed to Bring a New Medicine to Market, 2009-2018. *JAMA* **2020**, *323*, 844–853, DOI 10.1001/jama.2020.1166.
- (2) Mullard, A \$1.3 billion per drug? *Nature Reviews Drug Discovery* **2020**, *19*, 226, DOI 10.1038/d41573-020-00043-x.
- (3) Wouters, O J McKee, M Luyten, J Errors in Source Data for Study of Drug Development Costs. *JAMA* **2022**, *328*, 1110–1110, DOI 10.1001/jama.2022.14317.
- (4) Sertkaya, A Beleche, T Jessup, A Sommers, B D Costs of Drug Development and Research and Development Intensity in the US, 2000-2018. *JAMA Network Open* **2024**, *7*, e2415445–e2415445, DOI 10.1001/jamanetworkopen.2024.15445.
- (5) DiMasi, J A Grabowski, H G Hansen, R W Innovation in the pharmaceutical industry: New estimates of R&D costs. *Journal of Health Economics* **2016**, *47*, 20–33, DOI 10.1016/j.jhealeco.2016.01.012.
- (6) May, E Taylor, K Gupta, L Miranda, W In *Measuring the return from pharmaceutical innovation*; Deloitte Centre for Health Solutions: 2025.
- (7) Gangwal, A Lavecchia, A Unleashing the power of generative AI in drug discovery. *Drug Discovery Today* **2024**, *29*, 103992, DOI 10.1016/j.drudis.2024.103992.

- (8) Tang, X Dai, H Knight, E Wu, F Li, Y Li, T Gerstein, M A survey of generative AI for de novo drug design: new frontiers in molecule and protein generation. *Briefings in Bioinformatics* **2024**, *25*, bbae338, DOI 10.1093/bib/bbae338.
- (9) Gangwal, A Ansari, A Ahmad, I Azad, A K Kumarasamy, V Subramaniyan, V Wong, L S Generative artificial intelligence in drug discovery: basic framework, recent advances, challenges, and opportunities. *Frontiers in Pharmacology* **2024**, *15*, DOI 10.3389/fphar.2024.1331062.
- (10) Goodfellow, I J Pouget-Abadie, J Mirza, M Xu, B Warde-Farley, D Ozair, S Courville, A Bengio, Y In *Advances in Neural Information Processing Systems*, ed. by Ghahramani, Z Welling, M Cortes, C Lawrence, N Weinberger, K Curran Associates, Inc.: 2014; Vol. 27.
- (11) Tripathi, S Augustin, A I Dunlop, A Sukumaran, R Dheer, S Zavalny, A Haslam, O Austin, T Donchez, J Tripathi, P K Kim, E Recent advances and application of generative adversarial networks in drug discovery, development, and targeting. *Artificial Intelligence in the Life Sciences* **2022**, *2*, 100045, DOI 10.1016/j.aills.2022.100045.
- (12) Kotkondawar, R R Sutar, S R Kiwelekar, A W Kadam, V J Jadhav, S M A generative framework for enhancing drug target interaction prediction in drug discovery. *Scientific Reports* **2025**, *15*, 35588, DOI 10.1038/s41598-025-01589-9.
- (13) Amin, M H Andriyash, E Rolfe, J Kulchytsky, B Melko, R Quantum Boltzmann machine. *Physical Review X* **2018**, *8*, 021050, DOI 10.1103/PhysRevX.8.021050.
- (14) Liu, J.-G Wang, L Differentiable learning of quantum circuit born machines. *Physical Review A* **2018**, *98*, 062324, DOI 10.1103/PhysRevA.98.062324.
- (15) Barthe, A Grossi, M Vallecorsa, S Tura, J Dunjko, V Parameterized quantum circuits as universal generative models for continuous multivariate distributions. *npj Quantum Information* **2025**, *11*, 121, DOI 10.1038/s41534-025-01064-3.
- (16) Demidik, M Tüysüz, C Piatkowski, N Grossi, M Jansen, K Expressive equivalence of classical and quantum restricted Boltzmann machines. *Communications Physics* **2025**, *8*, 413, DOI 10.1038/s42005-025-02353-1.
- (17) Demidik, M Tüysüz, C Grossi, M Jansen, K Sample-based training of quantum generative models, arXiv:2511.11802 [quant-ph], 2025, DOI 10.48550/arXiv.2511.11802.
- (18) Mhiri, H Monbroussou, L Herrero-Gonzalez, M Thabet, S Kashefi, E Landman, J Constrained and Vanishing Expressivity of Quantum Fourier Models. *Quantum* **2025**, *9*, 1847, DOI 10.22331/q-2025-09-03-1847.
- (19) Jaderberg, B Gentile, A A Berrada, Y A Shishenina, E Elfving, V E Let quantum neural networks choose their own frequencies. *Physical Review A* **2024**, *109*, 042421, DOI 10.1103/PhysRevA.109.042421.
- (20) Xu, Y.-H Zhang, D.-B Frequency principle for quantum machine learning via Fourier analysis, arXiv:2409.06682 [quant-ph], 2025, DOI 10.48550/arXiv.2409.06682.
- (21) Duffy, C Jastrzebski, M Spectral Bias in Variational Quantum Machine Learning, arXiv:2506.22555 [quant-ph], 2025, DOI 10.48550/arXiv.2506.22555.
- (22) Dallaire-Demers, P.-L Killoran, N Quantum generative adversarial networks. *Physical Review A* **2018**, *98*, 012324, DOI 10.1103/physreva.98.012324.
- (23) Lloyd, S Weedbrook, C Quantum generative adversarial learning. *Physical review letters* **2018**, *121*, 040502, DOI 10.1103/PhysRevLett.121.040502.
- (24) Hu, L Wu, S.-H Cai, W Ma, Y Mu, X Xu, Y Wang, H Song, Y Deng, D.-L Zou, C.-L et al. Quantum generative adversarial learning in a superconducting quantum circuit. *Science advances* **2019**, *5*, eaav2761, DOI 10.1126/sciadv.aav2761.
- (25) Zoufal, C Lucchi, A Woerner, S Quantum generative adversarial networks for learning and loading random distributions. *npj Quantum Information* **2019**, *5*, 103, DOI doi.org/10.1038/s41534-019-0223-2.
- (26) Niu, M Y Zlokapa, A Broughton, M Boixo, S Mohseni, M Smelyanskiy, V Neven, H Entangling quantum generative adversarial networks. *Physical review letters* **2022**, *128*, 220505, DOI 10.1103/PhysRevLett.128.220505.
- (27) Chaudhary, S Huembeli, P MacCormack, I Patti, T L Kossaifi, J Galda, A Towards a scalable discrete quantum generative adversarial neural network. *Quantum Science and Technology* **2023**, *8*, 035002, DOI 10.1088/2058-9565/acc4e4.
- (28) Li, J Topaloglu, R O Ghosh, S Quantum Generative Models for Small Molecule Drug Discovery. *IEEE Transactions on Quantum Engineering* **2021**, *2*, 1–8, DOI 10.1109/TQE.2021.3104804.

- (29) Sikdar, D Cui, M Chau, A Bhamra, A Prasanna, S McMahan, L Hybrid Quantum-Classical Generative Adversarial Network for synthesizing chemically feasible molecules. *Journal of emerging investigations* **2023**, *6*, 1, DOI 10.59720/22-143.
- (30) Kao, P.-Y Yang, Y.-C Chiang, W.-Y Hsiao, J.-Y Cao, Y Aliper, A Ren, F Aspuru-Guzik, A Zhavoronkov, A Hsieh, M.-H Lin, Y.-C Exploring the Advantages of Quantum Generative Adversarial Networks in Generative Chemistry. *Journal of Chemical Information and Modeling* **2023**, *63*, 3307–3318, DOI 10.1021/acs.jcim.3c00562.
- (31) Anoshin, M Sagingalieva, A Mansell, C Zhiganov, D Shete, V Pflitsch, M Melnikov, A Hybrid Quantum Cycle Generative Adversarial Network for Small Molecule Generation. *IEEE Transactions on Quantum Engineering* **2024**, *5*, 1–14, DOI 10.1109/TQE.2024.3414264.
- (32) Arjovsky, M Chintala, S Bottou, L In *Proceedings of the 34th International Conference on Machine Learning*, ed. by Precup, D Teh, Y W PMLR 2017; Vol. 70, pp 214–223.
- (33) Gulrajani, I Ahmed, F Arjovsky, M Dumoulin, V Courville, A C In *Advances in Neural Information Processing Systems*, ed. by Guyon, I Luxburg, U V Bengio, S Wallach, H Fergus, R Vishwanathan, S Garnett, R Curran Associates, Inc.: 2017; Vol. 30.
- (34) Cao, N D Kipf, T MolGAN: An implicit generative model for small molecular graphs, arXiv:1805.11973 [stat.ML] 2022, DOI 10.48550/arXiv.1805.11973.
- (35) Ramakrishnan, R Dral, P O Rupp, M von Lilienfeld, O A Quantum chemistry structures and properties of 134 kilo molecules. *Scientific Data* **2014**, *1*, 140022, DOI 10.1038/sdata.2014.22.
- (36) Glavatskikh, M Leguy, J Hunault, G Cauchy, T Da Mota, B Dataset’s chemical diversity limits the generalizability of machine learning predictions. *Journal of Cheminformatics* **2019**, *11*, 69, DOI 10.1186/s13321-019-0391-2.
- (37) Polykovskiy, D et al. Molecular Sets (MOSES): A Benchmarking Platform for Molecular Generation Models. *Frontiers in Pharmacology* **2020**, *11*, DOI 10.3389/fphar.2020.565644.
- (38) Weininger, D SMILES, a chemical language and information system. 1. Introduction to methodology and encoding rules. *Journal of Chemical Information and Computer Sciences* **1988**, *28*, 31–36, DOI 10.1021/ci00057a005.
- (39) Prykhodko, O Johansson, S V Kotsias, P.-C Arús-Pous, J Bjerrum, E J Engkvist, O Chen, H A de novo molecular generation method using latent vector based generative adversarial network. *Journal of Cheminformatics* **2019**, *11*, 74, DOI 10.1186/s13321-019-0397-9.
- (40) Bravo-Prieto, C Baglio, J Cè, M Francis, A Grabowska, D M Carrazza, S Style-based quantum generative adversarial networks for Monte Carlo events. *Quantum* **2022**, *6*, 777, DOI 10.22331/q-2022-08-17-777.
- (41) Baglio, J Data augmentation experiments with style-based quantum generative adversarial networks on trapped-ion and superconducting-qubit technologies, arXiv:2405.04401 [quant-ph], 2024, DOI 10.48550/arXiv.2405.04401.
- (42) Karras, T Laine, S Aila, T A Style-Based Generator Architecture for Generative Adversarial Networks. *IEEE Transactions on Pattern Analysis and Machine Intelligence* **2021**, *43*, 4217–4228, DOI 10.1109/TPAMI.2020.2970919.
- (43) Chang, S Y Thanasilp, S Saux, B L Vallecorsa, S Grossi, M Latent Style-based Quantum GAN for high-quality Image Generation, arXiv:2406.02668 [quant-ph], 2024, DOI 10.48550/arXiv.2406.02668.
- (44) Liepelt, M Baglio, J Exponential capacity scaling of classical GANs compared to hybrid latent style-based quantum GANs, arXiv:2601.05036 [quant-ph], 2026, DOI 10.48550/arXiv.2601.05036.
- (45) Landrum, G RDKit: Open-Source Cheminformatics Software, 2025, DOI 10.5281/zenodo.16439048.
- (46) Irwin, J J Sterling, T Mysinger, M M Bolstad, E S Coleman, R G ZINC: A Free Tool to Discover Chemistry for Biology. *Journal of Chemical Information and Modeling* **2012**, *52*, 1757–1768, DOI 10.1021/ci3001277.
- (47) Benedetti, M Lloyd, E Sack, S Fiorentini, M Parameterized quantum circuits as machine learning models. *Quantum Science and Technology* **2019**, *4*, 043001, DOI 10.1088/2058-9565/ab4eb5.
- (48) Paszke, A et al. PyTorch: An Imperative Style, High-Performance Deep Learning Library. *arXiv e-prints* **2019**, arXiv:1912.01703, arXiv:1912.01703, DOI 10.48550/arXiv.1912.01703.

- (49) Bergholm, V Izaac, J Schuld, M et al. PennyLane: Automatic differentiation of hybrid quantum-classical computations. *arXiv preprint arXiv:1811.04968* **2018**.
- (50) Kandala, A Mezzacapo, A Temme, K et al. Hardware-efficient variational quantum eigensolver for small molecules and quantum magnets. *Nature* **2017**, *549*, 242–246, DOI 10.1038/nature23879.
- (51) Peruzzo, A McClean, J Shadbolt, P et al. A variational eigenvalue solver on a photonic quantum processor. *Nature Communications* **2014**, *5*, 4213, DOI 10.1038/ncomms5213.
- (52) Schuld, M Bocharov, A Svore, K M Wiebe, N Circuit-centric quantum classifiers. *Physical Review A* **2020**, *101*, DOI 10.1103/physreva.101.032308.
- (53) Wildman, S A Crippen, G M Prediction of Physicochemical Parameters by Atomic Contributions. *Journal of Chemical Information and Computer Sciences* **1999**, *39*, 868–873, DOI 10.1021/ci9903071.
- (54) Lipinski, C A Lombardo, F Dominy, B W Feeney, P J Experimental and computational approaches to estimate solubility and permeability in drug discovery and development settings1PII of original article: S0169-409X(96)00423-1. The article was originally published in *Advanced Drug Delivery Reviews* 23 (1997) 3–25.1. *Advanced Drug Delivery Reviews* **2001**, *46*, Special issue dedicated to Dr. Eric Tomlinson, *Advanced Drug Delivery Reviews*, A Selection of the Most Highly Cited Articles, 1991-1998, 3–26, DOI [https://doi.org/10.1016/S0169-409X\(00\)00129-0](https://doi.org/10.1016/S0169-409X(00)00129-0).
- (55) Lipinski, C A Lead- and drug-like compounds: the rule-of-five revolution. *Drug Discovery Today: Technologies* **2004**, *1*, 337–341, DOI <https://doi.org/10.1016/j.ddtec.2004.11.007>.
- (56) Kingma, D P Ba, J In *3rd International Conference on Learning Representations, ICLR 2015, San Diego, CA, USA, May 7-9, 2015, Conference Track Proceedings*, ed. by Bengio, Y LeCun, Y 2015.
- (57) Balló-Gimbernat, O Arroyo-Sánchez, M García-Molina, P Garriga, A Vilariño, F Shallow instantaneous quantum polynomial-time circuits for generative modeling on noisy intermediate-scale quantum hardware. *Phys. Rev. A* **2026**, *XX* DOI 10.1103/jcdk-q3xc.

## 1 SUPPLEMENTARY MATERIAL: INPUT DISTRIBUTIONS

In this section, the five main metrics are presented, calculated from the input train and test datasets. The plots are in Figure 12 and show certain differences between the two distributions, except for the LogP metric.

Table 7 then shows the mean internal diversity and the Wasserstein distance from the test sample.

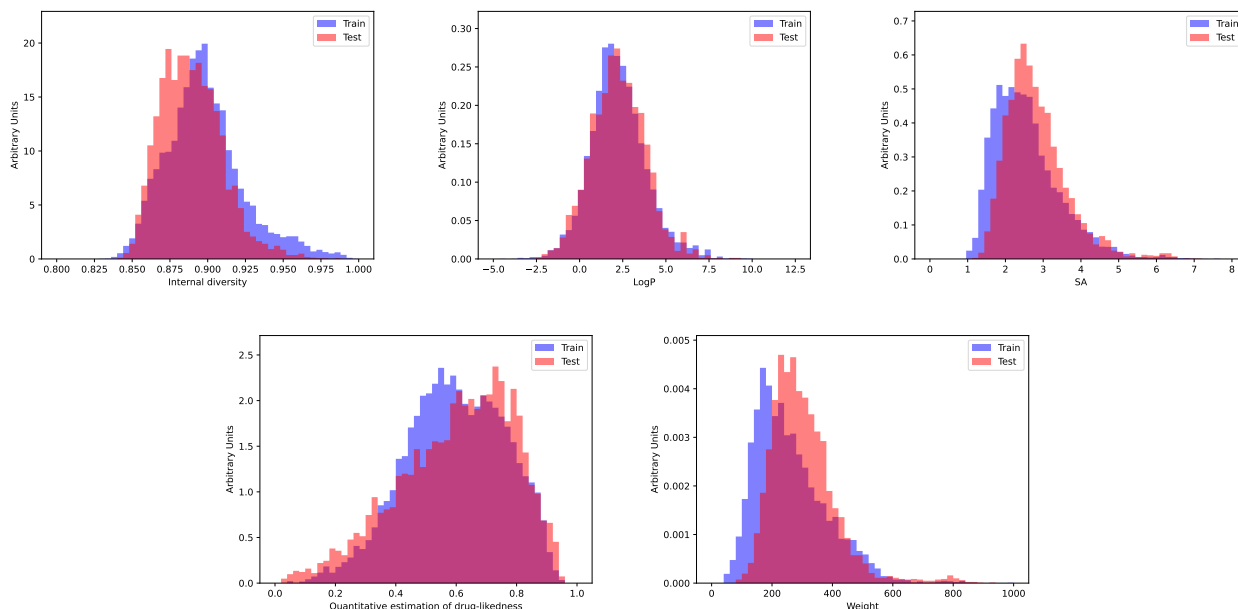


**Figure 12.** Comparison of metrics distributions between the input train and test sets.

Metrics	Train set	Test set
IntDiv	0.898	0.889
$\mathcal{W}(\text{LogP})$	0.091	—
$\mathcal{W}(\text{SA})$	0.268	—
$\mathcal{W}(\text{QED})$	0.027	—
$\mathcal{W}(\text{Weight})$	42.8	—

**Table 7.** Comparison of metrics between the input train and test sets.

## 2 SUPPLEMENTARY MATERIAL: VAE STUDY OF $N_{ep}$

In order to have a stable training of the model, the sensitivity of the loss function and metrics to the number of training epochs has to be studied. The general rule is that the loss function around the final chosen point of  $N_{ep}$  should be stable for the training as well as the test dataset.

Figure 13 presents the dependency of the loss function for both sets as a function of number of training epochs. From the requirement of stability it follows that anything below  $N_{ep} = 800$  might not be stable enough. Four working points have been chosen to test the hypothesis:

1.  $N_{ep} = 100$ : default value from the MOSES library;
2.  $N_{ep} = 250$ : value where the training set seems to be stable but the test set loss function is still increasing;

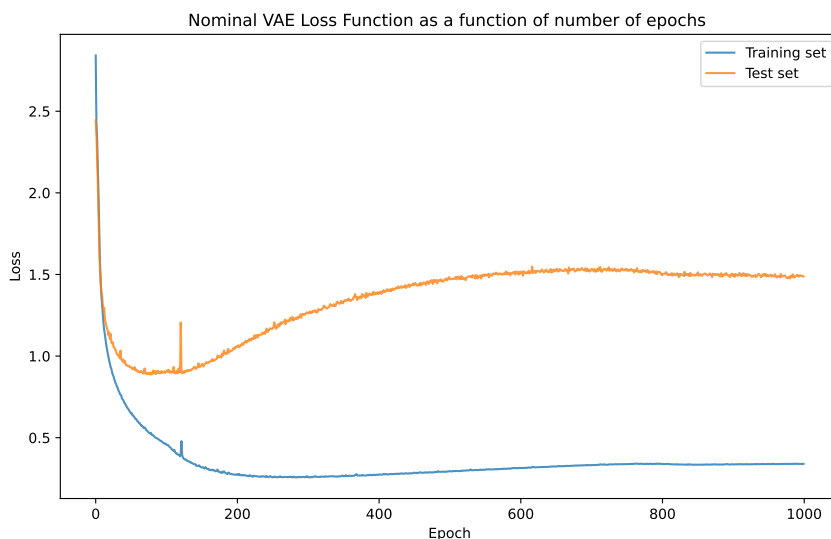


**Figure 13.** VAE loss function as a function of number of training epochs for the nominal VAE.

3.  $N_{ep} = 800$ : value where both loss functions seem to start to be stable;
4.  $N_{ep} = 1000$ : value chosen to be far from the beginning of the stable period of both loss functions.

The trainings have been performed for the four amounts of epochs and the results are summarized in Table 8. As expected, the values for the working point of 800 and 1,000 are consistent, hence supporting the theory that stable loss functions means stable metrics results and justifying the final choice of  $N_{ep} = 1,000$  for the VAE training. The same conclusion can be drawn from Figure 14 where an agreement is observed for the 800 and 1,000 working points while (in particular for internal diversity and molecular weight) the results for the 100 and 250 working points diverge.

$N_{ep}$	100	250	800	1,000
GPU runtime	9m 10s	17m 24s	48m 49s	52m 35s
IntDiv	0.892	0.919	0.896	0.896
$\mathcal{W}(\text{LogP})$	0.190	0.030	0.048	0.048
$\mathcal{W}(\text{SA})$	0.258	0.2646	0.2796	0.2751
$\mathcal{W}(\text{QED})$	0.084	0.090	0.096	0.097
$\mathcal{W}(\text{Weight})$	67.6	51.2	43.8	43.9

**Table 8.** VAE metrics comparison for the four  $N_{ep}$  points. The Wasserstein distance is measured between the test and generated samples. While the internal diversity is maximized, all other metrics are minimized. We also report the GPU runtime for comparison.

### 3 SUPPLEMENTARY MATERIAL: DEPENDENCY ON $N_{Gen}$

This section investigates the question whether 30,000 samples generated for the purpose of validation of the molecular sets is sufficient.

Once the sampler is called and generates the requested amount, a three-step efficiency estimation (as described in Section 2.3) is performed. The number of relevant molecules which are used to derive all the metrics is defined as:

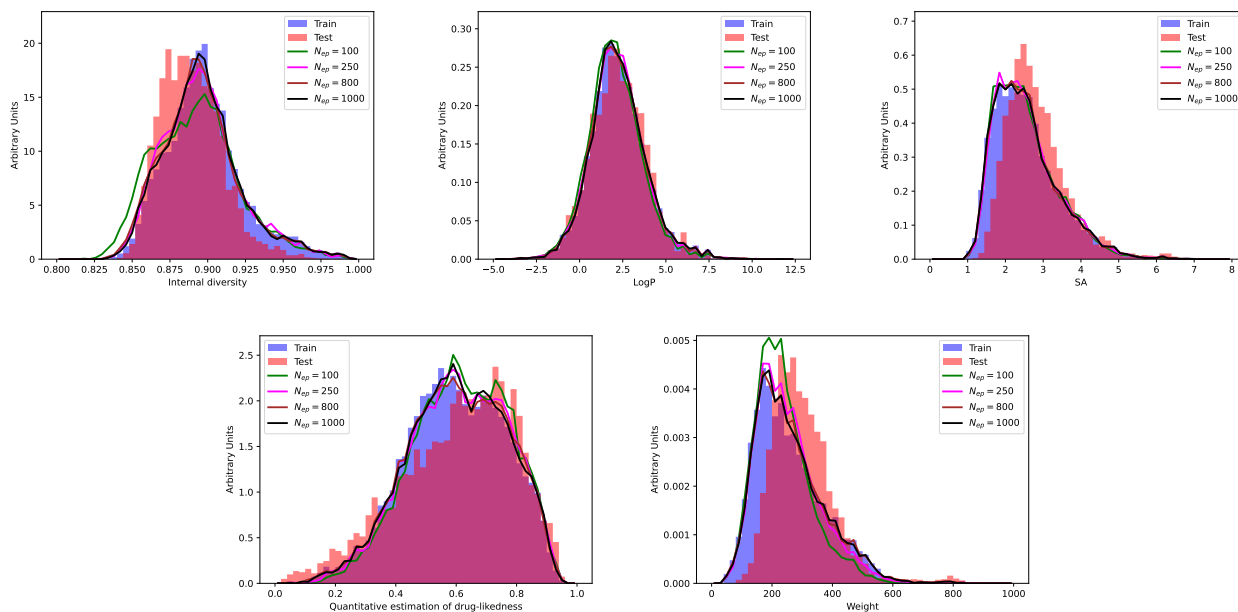


**Figure 14.** Metrics distributions for models trained with different number of epochs. Stabilization of the results starts with 800 epochs.

$$N_{Canonical} = N_{Generated} \times \epsilon_d \times \epsilon_v \times \epsilon_u \quad (6)$$

where  $\epsilon_d$  quantifies the amount of identically duplicated strings,  $\epsilon_v$  the amount of chemically valid molecules, and  $\epsilon_u$  the amount of canonically distinct molecules.

Table 9 presents the results for the nominal VAE settings and three different sizes of the generated sample. The trend of increasing inefficiency is clearly visible - while the amount of identical strings for the sample with 30,000 molecules (the 30k sample) is almost 50%, for the 1M set it is almost 90%. While the fraction of unique molecules stays almost constant, the fraction of valid molecules also drops with increasing number of generated samples significantly. The combined effect is then visible in the number of canonical generated molecules which, for a 33-fold increase in initial statistics, grew only by a factor of six.

Worth mentioning is also the observed trend in the novelty which dramatically increases. However, this increase does not immediately mean the increased capacity of generating new molecules. The novelty is defined as the number of generated molecules that were not present in the training sample. Although this holds well for the original MOSES analysis with more than 1M of molecules used for training, it is important to keep in mind that this analysis used only 12,000 molecules for training. That means that even if all training samples would be present in the 1M set, the novelty would be 83%. Same calculation for the 30k sample yields such minimal novelty of 6%. Comparing with the results from Table 9 we see that the 30k sample actually generates more new molecules than the 1M sample. The 30k scenario, resulting in about 13,000 valid canonical molecules is therefore a good candidate for a reliable novelty calculation in an analysis where only 12,000 training molecules are used.

All these arguments together with minimizing the sampling time lead to the decision of using 30,000 generated samples for subsequent result estimation.

## 4 SUPPLEMENTARY MATERIAL: VAE HYPERPARAMETER TUNING

The tuning of the VAE was performed for three distinct domains: the learning rate, the parameters of the encoder and parameters of the decoder. Tables 10, 11 and 12 present the parameter variations as well as the metrics comparison.

$N_{generated}$	30,000	300,000	1,000,000
GPU runtime	52m	1h 37m	2h 12m
Sampling runtime	10m	55m	1h 30m
$\epsilon_d$	0.479	0.168	0.120
$\epsilon_v$	0.889	0.704	0.609
$\epsilon_u$	0.996	0.982	0.977
$N_{Canonical}$	12,725	34,763	71,118
Novelty	0.237	0.662	0.835
IntDiv	0.896	0.896	0.895
$\mathcal{W}(\text{LogP})$	0.087	0.066	0.094
$\mathcal{W}(\text{SA})$	0.275	0.188	0.127
$\mathcal{W}(\text{QED})$	0.025	0.020	0.017
$\mathcal{W}(\text{Weight})$	43.9	38.4	32.6

**Table 9.** Metrics comparison for the nominal VAE training for three different sizes of sets of generated molecules. We also report runtime on the GPU.

	$3 \times 10^{-4}$	$1 \times 10^{-4}$	$1 \times 10^{-2}$	$5 \times 10^{-5}$	$5 \times 10^{-3}$	$1 \times 10^{-3}$
lr max	$3 \times 10^{-4}$	$1 \times 10^{-4}$	$1 \times 10^{-2}$	$5 \times 10^{-5}$	$5 \times 10^{-3}$	$1 \times 10^{-3}$
lr min	$3 \times 10^{-4}$	$1 \times 10^{-6}$	$1 \times 10^{-4}$	$5 \times 10^{-5}$	$5 \times 10^{-3}$	$1 \times 10^{-5}$
$\epsilon_d$	0.479	0.805	0.938	0.842	0.936	0.417
$\epsilon_v$	0.889	0.660	0.018	0.626	0.041	0.957
$\epsilon_u$	0.996	0.986	0.956	0.985	0.940	0.997
Novelty	0.237	0.702	0.925	0.768	0.856	0.119
IntDiv	0.896	0.893	0.887	0.891	0.929	0.898
$\mathcal{W}(\text{LogP})$	0.087	0.104	13.789	0.133	0.823	0.083
$\mathcal{W}(\text{SA})$	0.275	0.292	1.731	0.305	0.398	0.265
$\mathcal{W}(\text{QED})$	0.025	0.026	0.394	0.025	0.131	0.027
$\mathcal{W}(\text{Weight})$	43.9	57.3	1261.2	62.3	170.0	43.1

**Table 10.** Comparisons of the results of VAE learning rate tuning, the first column corresponds to the nominal scenario. Individual scenarios are defined by the learning rate minima/maxima at the top of the Table.

Table 10 and Figure 15 present the results of the learning rate optimization. It is obvious from the plots that when the learning rate is too large (0.01-0.0001 and 0.005 scenarios), the results collapse and the metrics become meaningless as it is reflected in Table 10. Comparison of the remaining scenarios prefers the 0.001-0.00001 tuning.

Table 11 and Figure 16 present the results of the encoder optimization. Although there seems to be a slight inclination to increase the hidden dimension to 512, changing the number of layers to two does not provide any improvement.

Table 12 and Figure 17 present the results of the decoder optimization. Contrary to the encoder, there seems to be a preference to increase the dropout to 0.75 and the number of layers to four, while the dimension of the hidden layer stays the same.

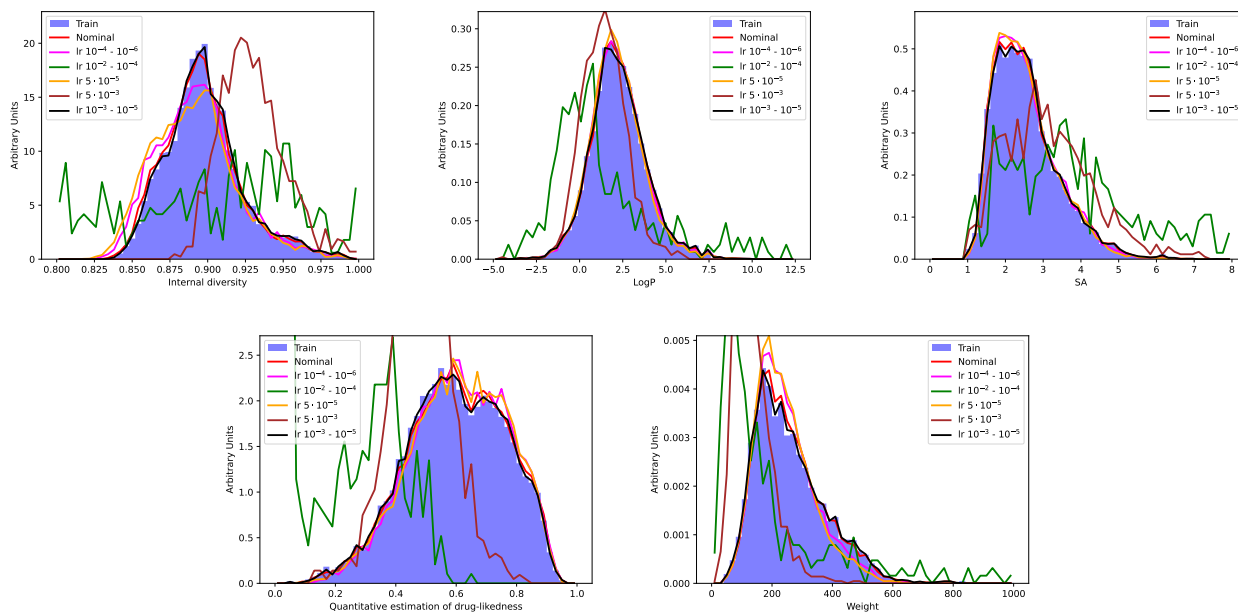


**Figure 15.** Metrics distributions for models trained with different learning rates. Clear breakdown for the 0.01-0.0001 and 0.005 scenarios is visible.

$n_l$	1	2	1	1
$D_h$	256	256	<b>128</b>	<b>512</b>
Dropout	0.0	<b>0.5</b>	0.0	0.0
$\epsilon_d$	0.479	0.548	0.475	0.5321
$\epsilon_v$	0.889	0.838	0.888	0.8552
$\epsilon_u$	0.996	0.994	0.995	0.9933
Novelty	0.237	0.349	0.238	0.327
IntDiv	0.896	0.895	0.896	0.896
$\mathcal{W}(\text{LogP})$	0.087	0.094	0.075	0.087
$\mathcal{W}(\text{SA})$	0.275	0.273	0.271	0.269
$\mathcal{W}(\text{QED})$	0.025	0.024	0.026	0.025
$\mathcal{W}(\text{Weight})$	43.9	44.3	43.6	45.3

**Table 11.** Comparisons of the results of VAE encoder parameter tuning, the first column corresponds to the nominal scenario. The scenario variation is highlighted at the top of the table. The dropout is active only for a scenario with more than one encoder layer, in such case value of 0.5 was used.

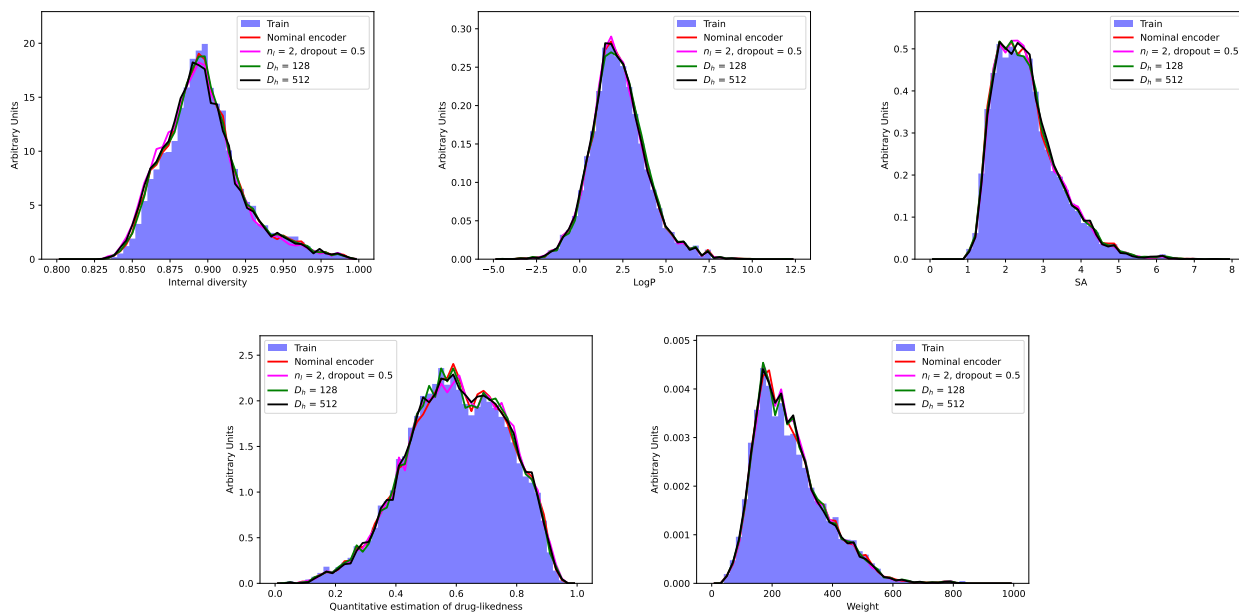


**Figure 16.** Metrics distributions for models trained with different encoder settings. Results are very similar between the different scenarios.

$n_l$	3	<b>2</b>	<b>4</b>	3	3	3	3
$D_h$	512	512	512	<b>256</b>	<b>1024</b>	512	512
Dropout	0.0	0.0	0.0	0.0	0.0	<b>0.25</b>	<b>0.75</b>
$\epsilon_d$	0.479	0.590	0.487	0.718	0.416	0.480	0.556
$\epsilon_v$	0.889	0.818	0.869	0.718	0.944	0.911	0.875
$\epsilon_v$	0.996	0.990	0.996	0.988	0.997	0.996	0.994
Novelty	0.237	0.429	0.240	0.573	0.126	0.248	0.378
IntDiv	0.896	0.896	0.897	0.894	0.898	0.897	0.896
$\mathcal{W}(\text{LogP})$	0.087	0.098	0.088	0.096	0.087	0.084	0.081
$\mathcal{W}(\text{SA})$	0.275	0.244	0.252	0.289	0.268	0.250	0.270
$\mathcal{W}(\text{QED})$	0.025	0.025	0.025	0.023	0.027	0.025	0.023
$\mathcal{W}(\text{Weight})$	43.9	48.4	41.7	51.3	45.3	42.6	43.6

**Table 12.** Comparisons of the results of VAE decoder parameter tuning, the first column corresponds to the nominal scenario. The scenario variation is highlighted at the top of the table. The default decoder dropout is zero regardless the number of layers.

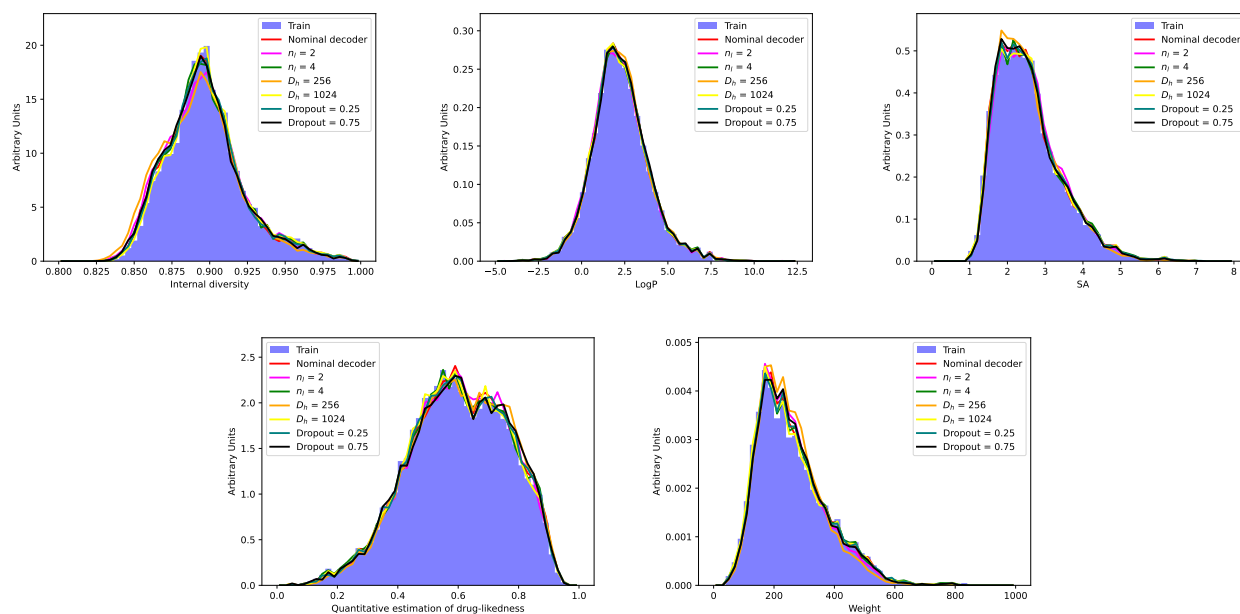


**Figure 17.** Metrics distributions for models trained with different decoder settings. Results are very similar for the different scenarios.

## 5 SUPPLEMENTARY MATERIAL: TEST OF THE VAE DECODER

In order to be able to claim that the VAE is functioning properly, it is important to test whether its decoding part is able to distinguish between different inputs. In other words, whether the decoder is sensitive to the shape of the distributions of the latent vectors or whether any distribution collapses to the same output.

The base latent space of dimension 10 was used and numbers drawn from the following distributions were decoded and processed using the standard metric evaluation:

1. The analysis training sample of 12,000 SMILES strings encoded by the VAE;
2. The analysis test sample of 4,087 SMILES strings encoded by the VAE;
3. 10,000 samples drawn from a uniform distribution between 0.0 and 1.0;
4. 10,000 samples drawn from a normal distribution with  $\mu = 0.0$  and  $\sigma = 1.0$ ;
5. 10,000 samples drawn from a log-normal distribution with  $\mu = 0.0$  and  $\sigma = 0.558$  shifted by two units to the negative values;
6. 10,000 samples drawn from a *sin* distribution with three peaks in the range  $[-3; 3]$ .

The distributions of the 10 vectors are presented in Figure 18 clearly showing the different shapes. The first two samples corresponding to the train and test encoded datasets exhibit similar behavior consistent with the normal(0;1) distribution, except for vectors number six and seven.

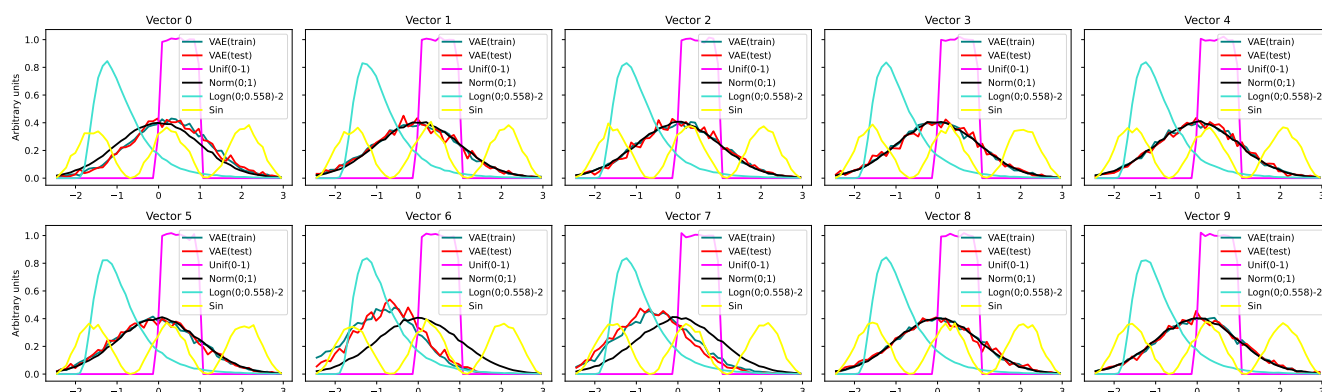


**Figure 18.** Distributions of 10 latent vectors used as inputs of the VAE decoder.

The sets of SMILES strings produced by the VAE decoder were subsequently evaluated in order to obtain the metrics. The comparison is in Figure 19.

The two shaded histograms correspond to the initial train and test samples without any use of VAE and clearly exhibit distinct behavior. However, the same samples, when encoded and decoded by the VAE (red and green), end up very consistent with each other but not with either the original train or test samples. This might hint at some level of information loss in the process of encoding and decoding the sample through a latent space of dimension only 10.

The VAE(gen) is very similar to the distribution originating from the uniform sampling in the latent space (brown and black). This is not very surprising because the internal MOSES VAE routine uses a uniform distribution as input for the sampler.

The uniform distribution has the most extreme shape difference with respect to the others (flat vs peak-y structure) and also shows the largest deviations in the distributions of the metrics. The VAE decoder seems to treat all distributions that exhibit a peak structure in a similar way.

Surprisingly, the metrics distribution originating in the log-normal scenario seems to be the most similar to the VAE(test) and VAE(gen) samples. That might be explained by the fact that the input distributions for vectors six and seven seem to be more consistent for the VAE(train) and VAE(test) with the log-normal

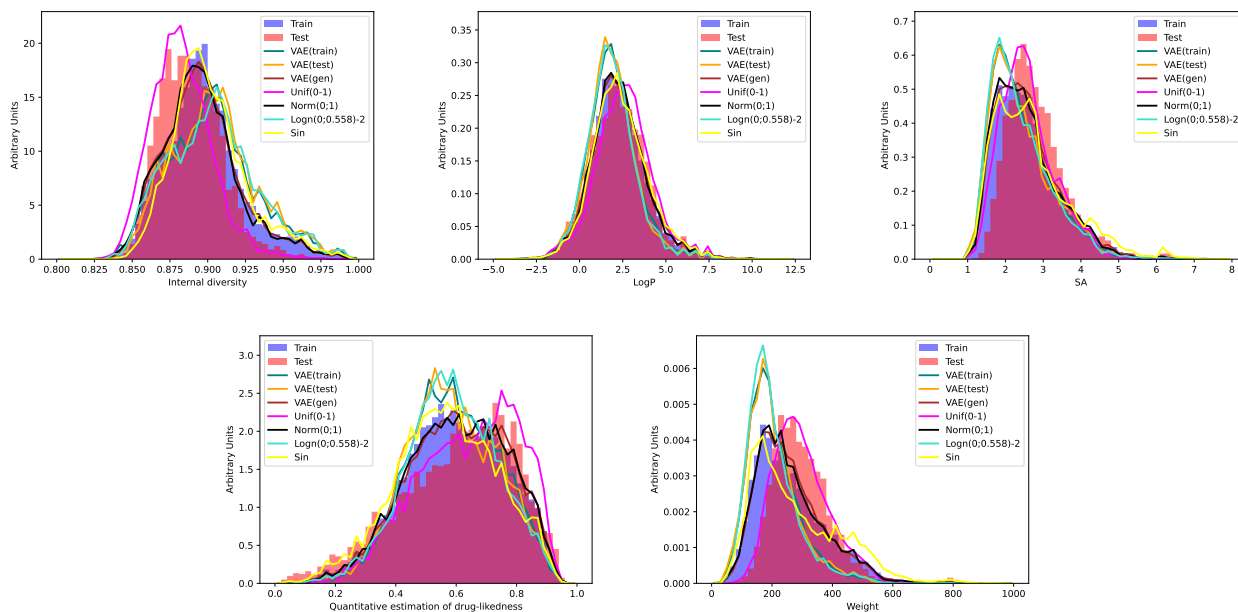


**Figure 19.** Metric distribution obtained from SMILES sets which were generated by the VAE decoder from various latent vector distributions. Additional scenario – VAE(gen) – corresponds to a set which is generated by the standard MOSES sampling procedure. The distributions are normalized to unit area.

rather than normal distributions. That would also hint that these two vectors are the ones with the largest discriminating power.

However, one can conclude that the VAE decoder is working as intended and is capable of producing SMILES sets with different feature characteristics depending on the shape of the latent vectors.

## 6 SUPPLEMENTARY MATERIAL: CORRELATIONS BETWEEN LATENT VECTORS

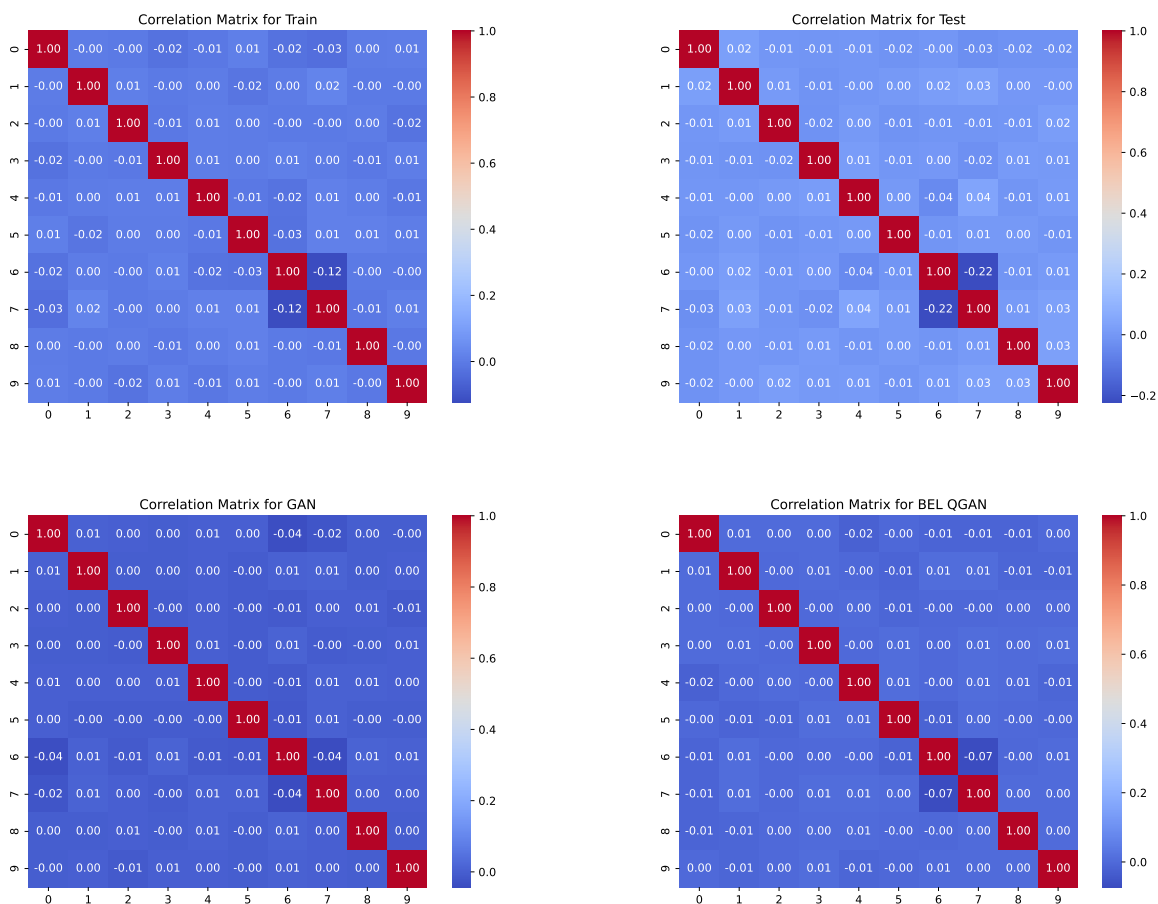
To complement the study of the latent space of dimension 10, this section presents the correlation matrices for the train, test, classical GAN, and QGAN datasets. While the train and test latent samples are simply a transformation of the SMILES sets through the VAE encoder, the samples for the GANs stem from the respective generators.

Figure 20 presents the correlation matrices. All vectors apart from numbers six and seven are almost perfectly uncorrelated, while the numbers six and seven shows a small level of anti-correlation. This effect has different size in the four samples and is manifested by differing distributions for the respective vectors as presented in Figure 9.

## 7 SUPPLEMENTARY MATERIAL: SUPPORTING MATERIAL FOR QGAN SCENARIOS

In this section, all detailed results supporting summary Table 5 are presented. Each of the following scenarios are represented by the corresponding metrics table and set of plots, for easy orientation, see Table 13.

All detailed results support the conclusion from Section 3.2. Tables 18 and 19 use the GAN with the corresponding latent dimension for comparison with the QGANs. The average statistical significance is well below one standard deviation and hence statistically compatible with the results from the scenario comparison Table 5.



**Figure 20.** Correlations between individual latent vectors for the training set, test set, classical GAN training output, and BEL QGAN training output, all for a latent dimension of 10.

Latent dimension	QGAN			Table	Figures
	$n_{qb}$	$n_l$	Readout		
10	5	2	Dual	14	8
10	5	4	Dual	15	21
10	10	2	Single	16	22
10	10	4, 6	Single	17	23
20	10	2	Dual	18	24
30	15	2	Dual	19	25
10, 20, 30	—	—	—	20	26

**Table 13.** Summary of the different scenarios and links to the corresponding individual tables and figures.

Metrics	Classical tuned	Styled simple QGAN	$Z_0$	styled BEL QGAN	$Z_0$
$N_{params}$	705,162	20		110	
$\epsilon_d$	$0.481 \pm 0.031$	$0.529 \pm 0.003$	+1.56	$0.523 \pm 0.003$	+1.36
$\epsilon_v$	$0.917 \pm 0.012$	$0.831 \pm 0.002$	-7.21	$0.875 \pm 0.003$	-3.43
$\epsilon_u$	$0.986 \pm 0.003$	$0.994 \pm 0.000$	+3.50	$0.993 \pm 0.001$	+2.90
Novelty	$0.536 \pm 0.015$	$0.572 \pm 0.003$	+2.40	$0.548 \pm 0.003$	+0.82
IntDiv	$0.898 \pm 0.004$	$0.882 \pm 0.000$	-4.60	$0.883 \pm 0.000$	-4.21
Filters	$0.721 \pm 0.011$	$0.737 \pm 0.003$	+1.43	$0.719 \pm 0.002$	-0.17
$\epsilon_{LogP}$	$0.898 \pm 0.007$	$0.883 \pm 0.001$	-2.35	$0.896 \pm 0.002$	-0.23
$\langle SA \rangle$	$2.391 \pm 0.080$	$2.575 \pm 0.007$	-2.31	$2.448 \pm 0.007$	-0.71
$\langle QED \rangle$	$0.599 \pm 0.007$	$0.641 \pm 0.001$	+6.17	$0.643 \pm 0.001$	+6.55
$\langle Weight \rangle$	$203.9 \pm 10.6$	$294.8 \pm 0.8$	-8.56	$261.4 \pm 0.8$	-5.42
$\langle Z_0 \rangle$	Reference	-	-1.00	-	-0.26

**Table 14.** Tuned classical GAN vs QGANs with  $n_{qb} = 5$ ,  $n_l = 2$ , and dual readout.

Metrics	Classical tuned	Styled simple QGAN	$Z_0$	Styled BEL QGAN	$Z_0$
$N_{params}$	705,162	40		210	
$\epsilon_d$	$0.481 \pm 0.031$	$0.526 \pm 0.003$	+1.46	$0.522 \pm 0.004$	+1.32
$\epsilon_v$	$0.917 \pm 0.012$	$0.830 \pm 0.002$	-7.24	$0.876 \pm 0.004$	-3.36
$\epsilon_u$	$0.986 \pm 0.003$	$0.994 \pm 0.000$	+3.42	$0.993 \pm 0.001$	+2.80
Novelty	$0.536 \pm 0.015$	$0.577 \pm 0.003$	+2.72	$0.548 \pm 0.004$	+0.76
IntDiv	$0.898 \pm 0.004$	$0.882 \pm 0.000$	-4.66	$0.883 \pm 0.000$	-4.21
Filters	$0.721 \pm 0.011$	$0.740 \pm 0.003$	+1.64	$0.719 \pm 0.003$	-0.12
$\epsilon_{LogP}$	$0.898 \pm 0.007$	$0.882 \pm 0.003$	-2.29	$0.896 \pm 0.002$	-0.36
$\langle SA \rangle$	$2.391 \pm 0.080$	$2.587 \pm 0.007$	-2.45	$2.450 \pm 0.006$	-0.74
$\langle QED \rangle$	$0.599 \pm 0.007$	$0.641 \pm 0.001$	+6.11	$0.644 \pm 0.001$	+6.61
$\langle Weight \rangle$	$203.9 \pm 10.6$	$297.4 \pm 0.6$	-8.82	$261.2 \pm 0.5$	-5.41
$\langle Z_0 \rangle$	Reference	-	-1.01	-	-0.27

**Table 15.** Tuned classical GAN vs QGANs with  $n_{qb} = 5$ ,  $n_l = 4$ , and dual readout.

Metrics	Classical tuned	Styled simple QGAN	$Z_0$	Styled BEL QGAN	$Z_0$
$N_{params}$	716,692	40		220	
$\epsilon_d$	$0.481 \pm 0.031$	$0.514 \pm 0.004$	+1.06	$0.514 \pm 0.002$	+1.06
$\epsilon_v$	$0.917 \pm 0.012$	$0.833 \pm 0.003$	-6.99	$0.887 \pm 0.003$	-2.45
$\epsilon_u$	$0.986 \pm 0.003$	$0.994 \pm 0.000$	+3.27	$0.992 \pm 0.001$	+2.45
Novelty	$0.536 \pm 0.015$	$0.586 \pm 0.003$	+3.34	$0.548 \pm 0.002$	+0.82
IntDiv	$0.898 \pm 0.004$	$0.882 \pm 0.000$	-4.68	$0.884 \pm 0.000$	-3.99
Filters	$0.721 \pm 0.011$	$0.737 \pm 0.003$	+1.40	$0.712 \pm 0.004$	-0.70
$\epsilon_{LogP}$	$0.898 \pm 0.007$	$0.885 \pm 0.002$	-1.91	$0.900 \pm 0.001$	+0.30
$\langle SA \rangle$	$2.391 \pm 0.080$	$2.569 \pm 0.005$	-2.23	$2.415 \pm 0.007$	-0.30
$\langle QED \rangle$	$0.599 \pm 0.007$	$0.645 \pm 0.001$	+6.81	$0.641 \pm 0.001$	+6.19
$\langle Weight \rangle$	$203.9 \pm 10.6$	$293.6 \pm 1.1$	-8.43	$250.1 \pm 0.9$	-4.36
$\langle Z_0 \rangle$	Reference	-	-0.84	-	-0.10

**Table 16.** Tuned classical GAN vs QGANs with  $n_{qb} = 10$ ,  $n_l = 2$ , and single readout.

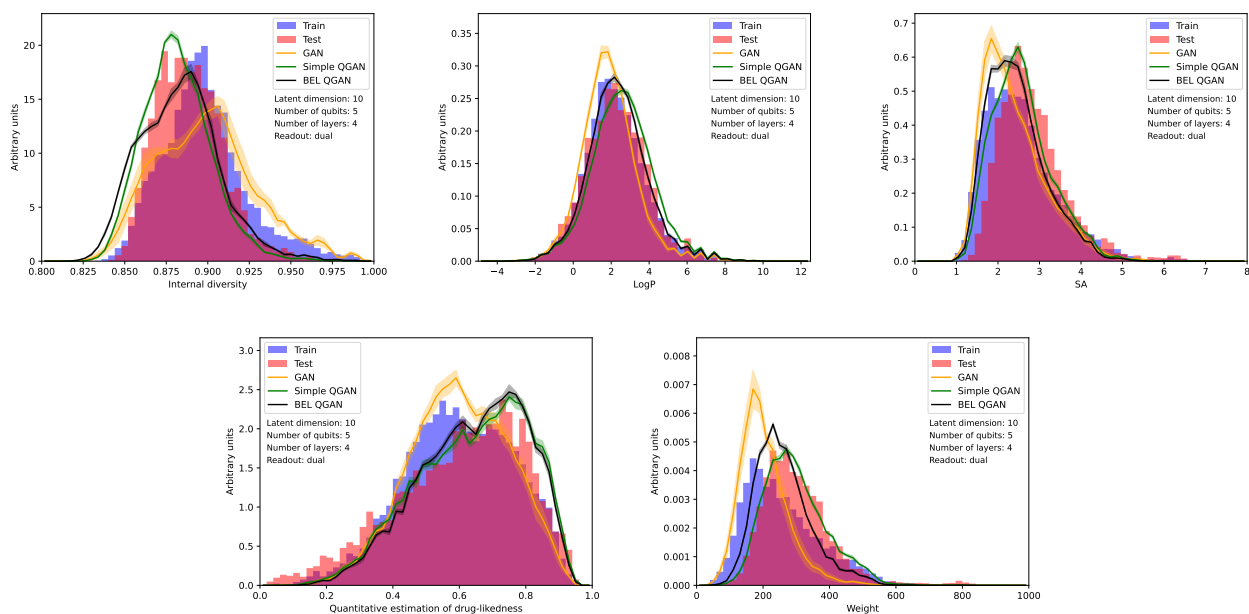


**Figure 21.** Metrics distributions for classical and quantum models. All GANs are trained with a latent dimension of 10. The quantum GANs use  $n_{qb} = 5$ ,  $n_l = 4$ , and dual readout.

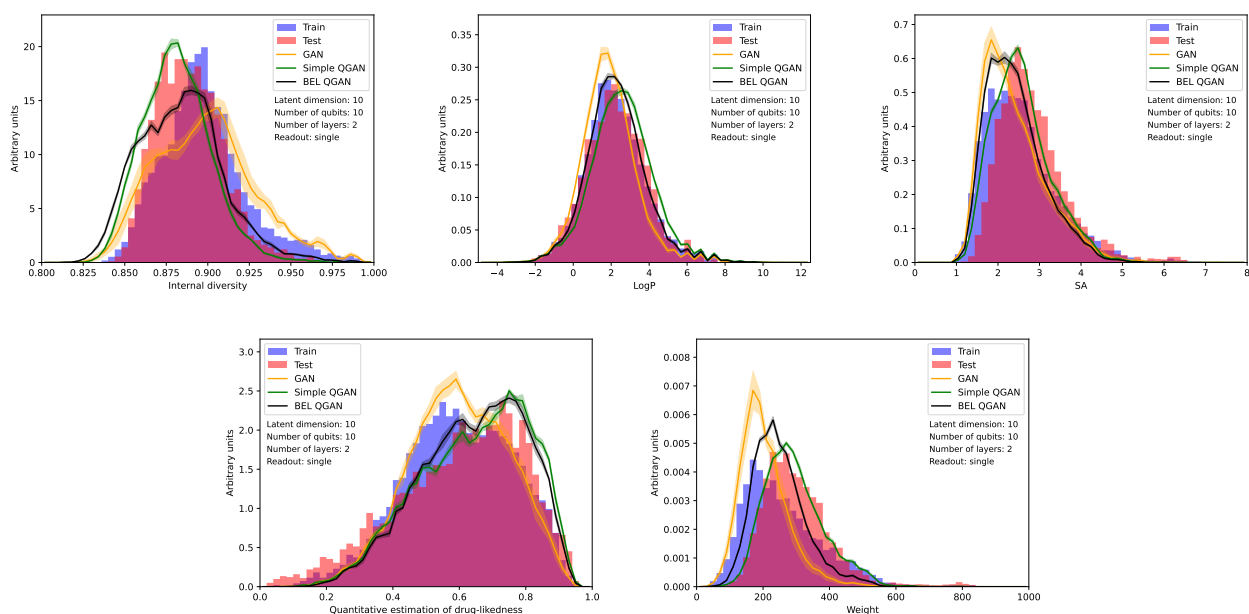


**Figure 22.** Metrics distributions for classical and quantum models. All GANs are trained with a latent dimension of 10. The quantum GANs use  $n_{qb} = 10$ ,  $n_l = 2$ , and single readout.

Metrics	Classical tuned	Styled simple QGAN	$Z_0$	Styled BEL QGAN	$Z_0$	styled BEL	$Z_0$
$n_l$	-	4		4		6	
$N_{params}$	705,162	80		420		620	
$\epsilon_d$	$0.481 \pm 0.031$	$0.515 \pm 0.005$	+1.08	$0.516 \pm 0.005$	+1.13	$0.515 \pm 0.003$	+1.10
$\epsilon_v$	$0.917 \pm 0.012$	$0.833 \pm 0.002$	-6.95	$0.887 \pm 0.003$	-2.42	$0.888 \pm 0.002$	-2.41
$\epsilon_u$	$0.986 \pm 0.003$	$0.994 \pm 0.000$	+3.26	$0.992 \pm 0.001$	+2.48	$0.992 \pm 0.001$	+2.62
Novelty	$0.536 \pm 0.015$	$0.586 \pm 0.002$	+3.37	$0.549 \pm 0.002$	+0.87	$0.550 \pm 0.001$	+0.93
IntDiv	$0.898 \pm 0.004$	$0.882 \pm 0.000$	-4.69	$0.884 \pm 0.000$	-4.01	$0.884 \pm 0.000$	-3.99
Filters	$0.721 \pm 0.011$	$0.737 \pm 0.003$	+1.41	$0.714 \pm 0.002$	-0.56	$0.712 \pm 0.003$	-0.77
$\epsilon_{LogP}$	$0.898 \pm 0.007$	$0.885 \pm 0.003$	-1.87	$0.900 \pm 0.002$	+0.25	$0.897 \pm 0.002$	-0.11
$\langle SA \rangle$	$2.391 \pm 0.080$	$2.571 \pm 0.007$	-2.25	$2.417 \pm 0.011$	-0.32	$2.421 \pm 0.004$	-0.37
$\langle QED \rangle$	$0.599 \pm 0.007$	$0.645 \pm 0.001$	+6.83	$0.641 \pm 0.001$	+6.15	$0.641 \pm 0.001$	+6.23
$\langle Weight \rangle$	$203.9 \pm 10.6$	$293.7 \pm 1.2$	-8.44	$251.1 \pm 1.9$	-4.39	$249.9 \pm 0.9$	-4.33
$\langle Z_0 \rangle$	Reference	-	-0.83	-	-0.08	-	-0.11

**Table 17.** Tuned classical GAN vs QGANs with  $n_{qb} = 10$ ,  $n_l = 4, 6$ , and single readout.

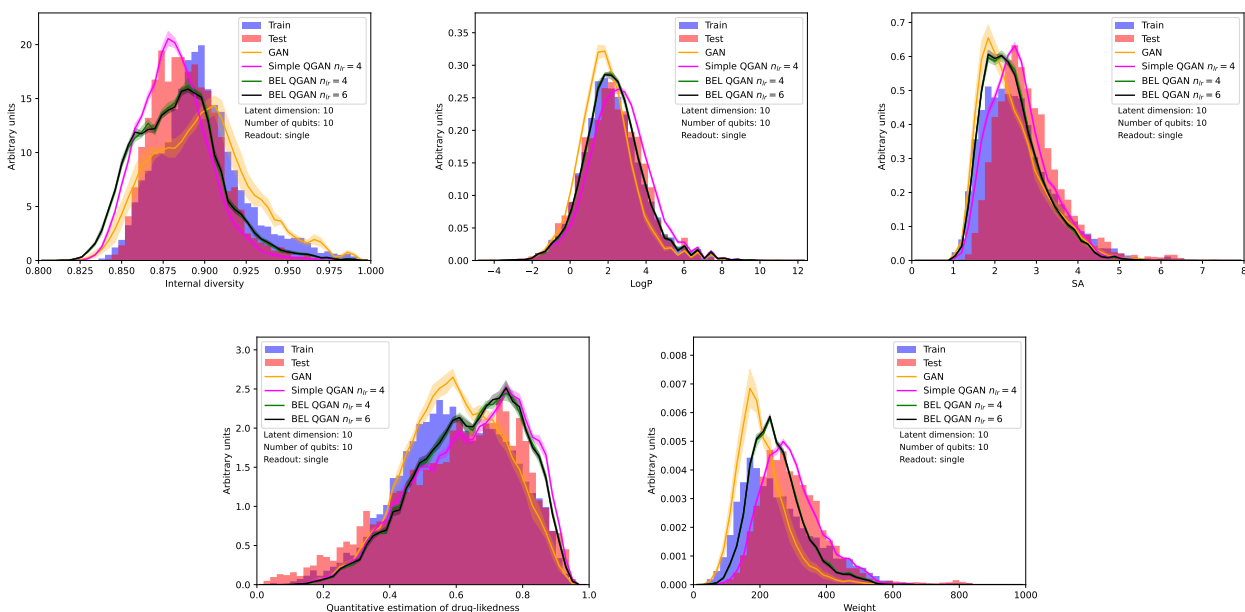


**Figure 23.** Metrics distributions for classical and quantum models. All GANs are trained with a latent dimension of 10. The quantum GANs use  $n_{qb} = 10$ ,  $n_l = 4$  and 6, and single readout.

Metrics	Classical tuned	Styled simple QGAN	$Z_0$	Styled BEL QGAN	$Z_0$
<b>Latent dimension</b>	20	20		20	
$N_{params}$	716,692	40		220	
$\epsilon_d$	$0.526 \pm 0.022$	$0.507 \pm 0.003$	-0.85	$0.519 \pm 0.005$	-0.32
$\epsilon_v$	$0.901 \pm 0.008$	$0.911 \pm 0.004$	+1.23	$0.910 \pm 0.002$	+1.22
$\epsilon_u$	$0.990 \pm 0.002$	$0.991 \pm 0.001$	+0.25	$0.991 \pm 0.001$	+0.05
Novelty	$0.488 \pm 0.018$	$0.484 \pm 0.001$	-0.22	$0.484 \pm 0.002$	-0.25
IntDiv	$0.893 \pm 0.002$	$0.890 \pm 0.000$	-1.42	$0.892 \pm 0.000$	-0.64
Filters	$0.724 \pm 0.004$	$0.720 \pm 0.002$	-0.88	$0.722 \pm 0.003$	-0.56
$\epsilon_{LogP}$	$0.897 \pm 0.004$	$0.900 \pm 0.002$	+0.69	$0.897 \pm 0.003$	+0.11
$\langle SA \rangle$	$2.446 \pm 0.034$	$2.393 \pm 0.004$	+1.56	$2.421 \pm 0.003$	+0.75
$\langle QED \rangle$	$0.613 \pm 0.006$	$0.620 \pm 0.001$	+1.24	$0.618 \pm 0.001$	+0.93
$\langle Weight \rangle$	$234.4 \pm 11.7$	$231.7 \pm 0.9$	+0.23	$233.4 \pm 0.7$	+0.09
$\langle Z_0 \rangle$	Reference	-	+0.18	-	+0.14

**Table 18.** Quantum GANs with latent dimension of 20,  $n_{qb} = 10$ ,  $n_l = 2$ , and dual readout.

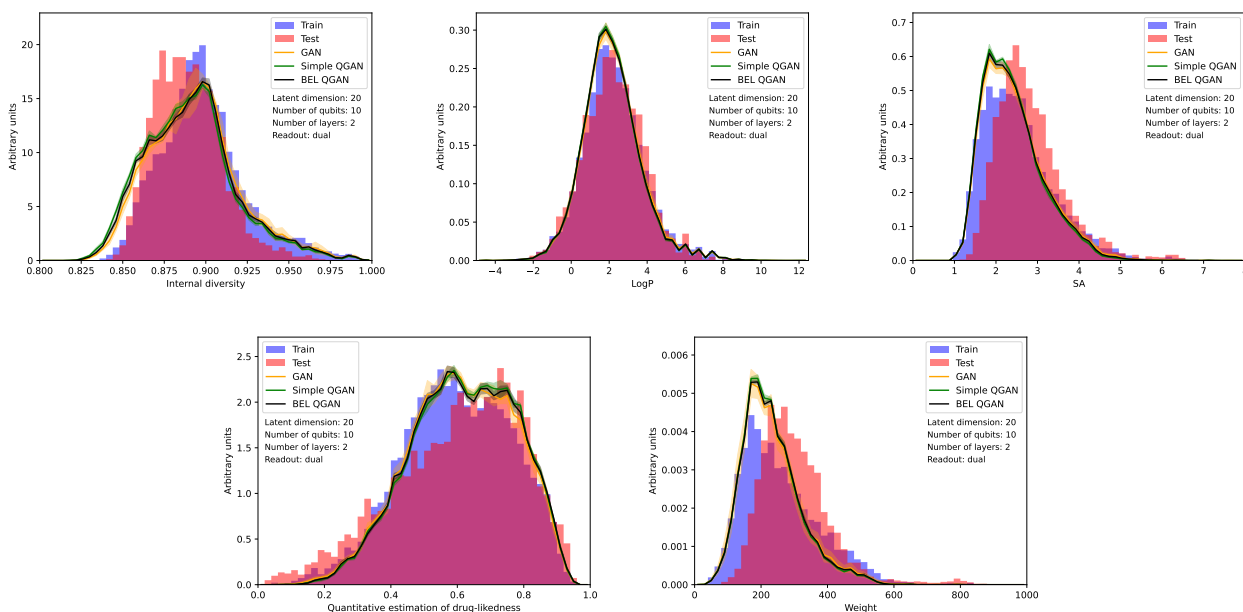


**Figure 24.** Metrics distributions for classical and quantum models. All GANs are trained with a latent dimension of 20. The quantum GANs use  $n_{qb} = 10$ ,  $n_l = 2$ , and dual readout.

Metrics	Classical tuned	Styled simple QGAN	$Z_0$	Styled BEL QGAN	$Z_0$
<b>Latent dimension</b>	30	30		30	
$N_{params}$	728,222	60		330	
$\epsilon_d$	$0.500 \pm 0.066$	$0.496 \pm 0.003$	-0.06	$0.504 \pm 0.002$	+0.07
$\epsilon_v$	$0.884 \pm 0.032$	$0.895 \pm 0.002$	+0.32	$0.903 \pm 0.003$	+0.57
$\epsilon_u$	$0.990 \pm 0.004$	$0.992 \pm 0.001$	+0.42	$0.991 \pm 0.001$	+0.39
Novelty	$0.504 \pm 0.018$	$0.476 \pm 0.003$	-1.55	$0.471 \pm 0.003$	-1.81
IntDiv	$0.896 \pm 0.003$	$0.888 \pm 0.000$	-2.57	$0.891 \pm 0.000$	-1.75
Filters	$0.719 \pm 0.015$	$0.725 \pm 0.002$	+0.38	$0.723 \pm 0.003$	+0.25
$\epsilon_{LogP}$	$0.894 \pm 0.012$	$0.901 \pm 0.002$	+0.55	$0.900 \pm 0.002$	+0.44
$\langle SA \rangle$	$2.451 \pm 0.144$	$2.349 \pm 0.002$	+0.71	$2.367 \pm 0.005$	+0.59
$\langle QED \rangle$	$0.604 \pm 0.006$	$0.624 \pm 0.001$	+3.23	$0.619 \pm 0.001$	+2.34
$\langle Weight \rangle$	$225.8 \pm 30.1$	$232.8 \pm 0.5$	-0.23	$226.8 \pm 0.9$	-0.03
$\langle Z_0 \rangle$	Reference	-	+0.12	-	+0.11

**Table 19.** Quantum GANs with a latent dimension of 30,  $n_{qb} = 15$ ,  $n_l = 2$ , and dual readout.

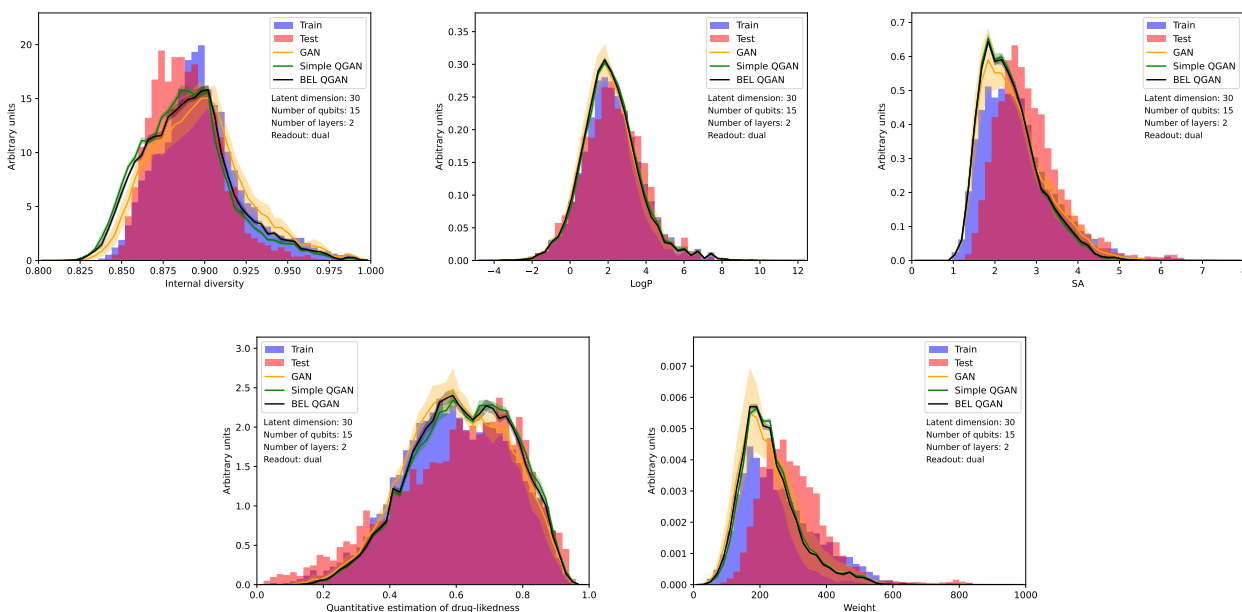


**Figure 25.** Metrics distributions for classical and quantum models. All GANs are trained with a latent dimension of 30. The quantum GANs use  $n_{qb} = 15$ ,  $n_l = 2$ , and dual readout.

Latent Dimension	10	20	$Z_0$	30	$Z_0$
$N_{params}$	705, 162	716, 692		728, 222	
$\epsilon_d$	$0.481 \pm 0.031$	$0.526 \pm 0.022$	+1.19	$0.500 \pm 0.066$	+0.25
$\epsilon_v$	$0.917 \pm 0.012$	$0.901 \pm 0.008$	-1.16	$0.884 \pm 0.032$	-0.96
$\epsilon_u$	$0.986 \pm 0.003$	$0.990 \pm 0.002$	+1.59	$0.990 \pm 0.004$	+0.84
Novelty	$0.536 \pm 0.015$	$0.488 \pm 0.018$	-2.04	$0.504 \pm 0.018$	-1.39
IntDiv	$0.898 \pm 0.004$	$0.893 \pm 0.002$	-1.19	$0.896 \pm 0.003$	-0.43
Filters	$0.721 \pm 0.011$	$0.724 \pm 0.004$	+0.28	$0.719 \pm 0.015$	-0.07
$\epsilon_{LogP}$	$0.898 \pm 0.007$	$0.897 \pm 0.004$	-0.14	$0.894 \pm 0.012$	-0.26
$\langle SA \rangle$	$2.391 \pm 0.080$	$2.446 \pm 0.034$	-0.64	$2.451 \pm 0.144$	-0.36
$\langle QED \rangle$	$0.599 \pm 0.007$	$0.613 \pm 0.006$	+1.54	$0.604 \pm 0.006$	+0.49
$\langle \text{Weight} \rangle$	$203.9 \pm 10.6$	$234.4 \pm 11.7$	-1.94	$225.8 \pm 30.1$	-0.69
$\langle Z_0 \rangle$	Reference	-	-0.25	-	-0.26

**Table 20.** Classical GAN comparison of different latent dimensions.

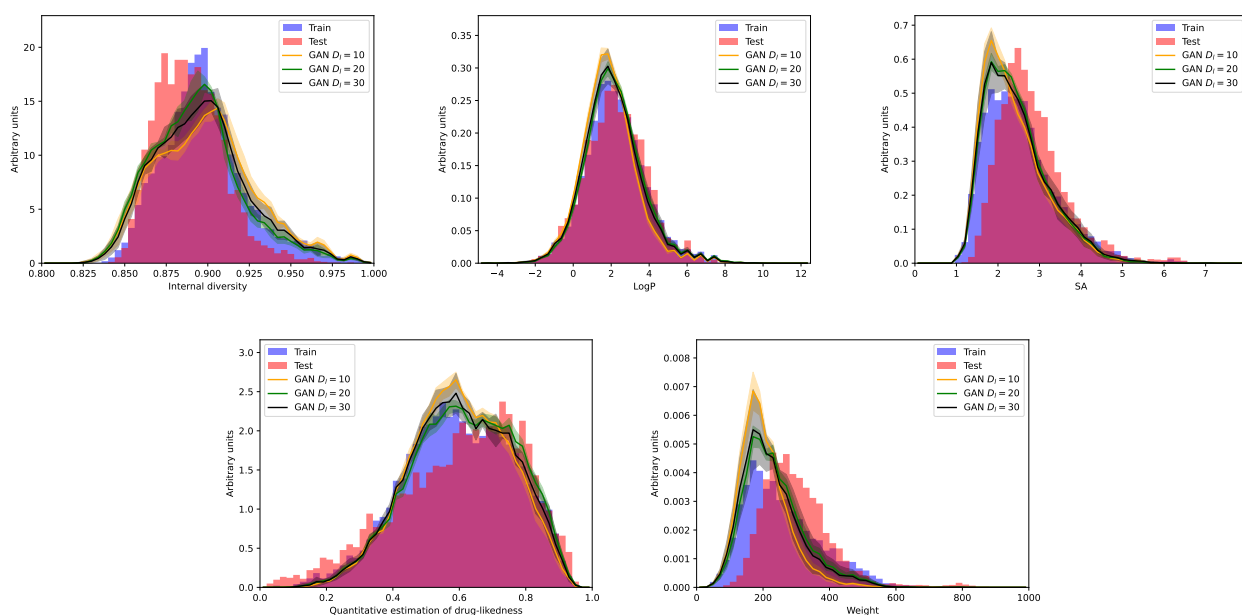


**Figure 26.** Metrics distributions for classical models trained with different latent dimensions.